Onset of three-dimensionality in supersonic flow over a slender double wedge

Sidharth GS,* Anubhav Dwivedi, Graham V. Candler, and Joseph W. Nichols
Aerospace Engineering and Mechanics, University of Minnesota, Minneapolis, Minnesota 55455, USA

(Received 26 February 2018; published 19 September 2018)

We investigate the onset of three-dimensionality in a Mach 5 slender-double-wedge flow as the turn angle at the compression corner increases. Beyond a critical angle, the two-dimensional flow destabilizes to three-dimensional perturbations and results in growth of spanwise periodic flow structures. We carry out global linear stability analysis to identify the critical turn angle and the nature of the associated three-dimensional instability. At the critical angle, an unstable mode is present in the separation bubble and the reattached boundary layer. The mode is associated with streamwise streaks in wall temperature downstream of the corner. The existence of the unstable mode and its growth rate are confirmed with direct numerical simulations. It is found from budget analysis that streamwise deceleration of the recirculating flow plays a dominant role in the three-dimensional instability. Wave-maker analysis suggests that the instability does not have a centrifugal origin. Linear stability analysis of the steady-state flow at an angle beyond bifurcation is also carried out. The spanwise wavelength of the most unstable mode obtained at this turn angle compares well with experimental observations.

DOI: 10.1103/PhysRevFluids.3.093901

I. INTRODUCTION

High-speed flow over a double wedge is a canonical case of shock–boundary-layer interaction [1]. Flow deflection at the compression corner can cause the laminar boundary layer to separate due to inviscid pressure rise. This is associated with a separation-reattachment shock system. A strong turn angle at the corner can cause an incoming laminar boundary layer to become turbulent post reattachment [2]. Experiments of supersonic and hypersonic flow on compression ramps and double wedges exhibit three-dimensionality in the form of streamwise striations or streaks in wall temperature near reattachment, which persist downstream. Streamwise vortical structures associated with these streaks result in heat transfer with large local peaks in the span. The three-dimensional flow structures have a destabilizing effect on the boundary layer and play a role in the transition process [3,4].

Streamwise streaks are observed in compression corner experiments over a range of Mach numbers, turn angles, and wall temperatures [2,5–9]. The presence of streaks near reattachment is not restricted to compression ramps [3]. For example, they also appear in axisymmetric geometries such as the hollow cylinder flare [10] and oblique shock–boundary-layer interaction [11]. The wavelength associated with the streamwise streaks is usually on the order of twice the boundary-layer thickness at reattachment [2,12]. De Luca *et al.* [13] and de la Chevalerie *et al.* [14] studied the role of the unit Reynolds number and the leading edge to corner distance on the spanwise wavelength of the streaks on a Mach 7 15° compression ramp. The wavelength was found to decrease with increasing unit Reynolds number and with decreasing flat-plate length. Roghelia *et al.* [2] found that increasing the radius of curvature of the flat-plate leading edge for a Mach 8 15° ramp

*Corresponding author: sidharth_gs@hotmail.com

increases the wavelength of the streaks on account of the thicker boundary layer. This suggests that the wavelength of the streamwise vortices scales with the local boundary-layer thickness.

The observed streaks are often attributed to Görtler-like vortices [15] that arise from destabilizing centrifugal forces near reattachment where the streamline curvature is highly concave. Görtler instability implies a role of upstream perturbations [16] in the formation of streaks. Therefore, some studies have proposed leading edge imperfections as the origin of streamwise streaks. However, Matsumura *et al.* [17] studied streamwise vortices on a scramjet forebody geometry and mentioned that streamwise streaks appear on HyperX even with a high-quality leading edge. Roghelia *et al.* [18] demonstrated a similar spanwise heat flux pattern on two different 15° ramps in two different experimental facilities. Zhuang *et al.* [19] visualized a Mach 3 turbulent boundary-layer turning on a 25° compression ramp using nanotracer planar laser scattering and found that Görtler-like streamwise vortices are present not only at the reattachment but in the entire separation bubble. Priebe and Martín [20] and Priebe *et al.* [21] analyzed a Mach 2.9 turbulent boundary-layer turning at a 24° corner and conjectured the presence of a global instability associated with the observed streamwise vortices. Brown *et al.* [22] carried out three-dimensional simulations of a Mach 11 cylinder flare and reported that the three-dimensionality in the separation bubble can result in the formation of heat flux streaks near reattachment independently of the Görtler instability of the reattaching shear layer. Therefore, instabilities in the separation bubble and their connection to streamwise streaks post reattachment merit attention.

Literature on high-speed compression ramp flow instabilities is scarce. Inger [12] first explained the presence of three-dimensional counterrotating vortices at reattachment as a steady neutral perturbation that can exist in reattaching flow idealized as a Hiemenz-type stagnation point flow. The work is similar to the Görtler-Hämmerlin analysis [23,24], where the stability of flat-plate stagnation flow is investigated with respect to three-dimensional perturbations. Fletcher *et al.* [25] and Cassel *et al.* [26] used the unsteady supersonic triple-deck equations to discover the presence of a two-dimensional instability in the recirculation region beyond a critical ramp angle.

Several studies have focused on three-dimensional instabilities in oblique shock–boundary-layer interaction. Oblique shock interaction is similar to compression ramp interaction, although a major difference is the presence of an impinging shock in the former case. The inviscid flow turns once on the compression ramp, but twice in the presence of an oblique shock impinging on the wall. Dwivedi *et al.* [27] used adjoint-based optimization to obtain streaklike perturbations that can rapidly amplify post reattachment. However, the analysis was restricted to the reattached boundary layer and did not consider reversed flow in the separation bubble. Global stability methods [28] that can account for flow recirculation have also been applied to oblique shock–boundary-layer interaction. Global linear stability considers the linear stability of small-amplitude perturbations superposed on a steady base flow state without assumptions on the spatial variation of the base flow and the directionality of perturbation waves. This makes global analysis suitable for investigating the stability of separated flows. Robinet [29] and Hildebrand *et al.* [30] have applied global stability analysis to study the bifurcation of the nominally two-dimensional interaction to three-dimensionality in Mach 2.15 and Mach 5.92 interactions, respectively. In the Mach 5.92 case [30], corrugation in the impinging shock foot was found to play a role in the physical mechanism sustaining the three-dimensional instability. Global stability analysis has also been used in the past to study the onset of three-dimensional instability in an incompressible separation bubble [31–33], backward facing step [34], and open cavity flows [35]. In these stability analyses, when the strength of the two-dimensional recirculation increases beyond a critical value, a three-dimensional instability causes topological changes in the flow [31].

We apply global stability analysis to shock–boundary-layer interaction on a slender double wedge. Experimental visualization of regularly spaced streaks on a nominally two-dimensional flow field over a double wedge suggests the existence of an unstable spanwise periodic perturbation. Since the streaks are not related to finite span effects [4], the physical system presents itself as an ideal candidate for global stability analysis where perturbations are assumed to be periodic in the span. We consider slender double wedges where the flow turn angle at both ramps is small, close to

10°. This is important for two reasons. First, the inviscid shock structure changes from Edney type VI to Edney type V/IV/IVr [1] with increasing turn angle. Therefore, small- and large-turn-angle regimes involve fundamentally different inviscid-viscous interaction. Second, on double wedges with large first ramp turn angle, the two-dimensional boundary layer can be susceptible to large three-dimensional perturbation growth prior to separation [36,37]. In the double-ramp experiments by Caljouw [36], this growth is visualized via oil flow and temperature-sensitive paint as streaks upstream of the interaction. The physical system then may no longer be simply hypothesized to have originated from a globally unstable mode of the steady-state two-dimensional flow field. The boundary layer undergoing separation in such a case is already three-dimensional due to the growth of external perturbations and results in a recirculation bubble different from a two-dimensional steady recirculation.

Moreover, if the two-dimensional steady-state flow is unstable to two-dimensional perturbations [38,39], it is nontrivial to compute it from a numerical standpoint. Therefore, we investigate the *intrinsic* three-dimensionality [40] in the slender-double-wedge flow and the associated wall temperature streak patterns. Perturbations originating upstream of the separating boundary layer are absent in this analysis and Görtler-like instability at separation or reattachment is not considered. The low-pass spatiotemporal amplification properties of the recirculation bubble with respect to *extrinsic* perturbations have been investigated in the case of oblique shock–boundary-layer interaction by Sansica *et al.* [41,42] and in the slender-double-wedge interaction by Dwivedi *et al.* [43].

Although the present work investigates the flow on a slender double wedge, the findings in this paper also apply to a flat-plate compression ramp. This was demonstrated in Ref. [40], where the experiment of Bleilebens and Olivier [9] on a heated flat-plate compression ramp was considered. Here we focus on a double wedge because the reference experiment [7] incorporated a long test time of 7 s, which is relevant to the asymptotic stability of the shock–boundary-layer interaction.

The paper is organized as follows. In Sec. II we linearize the compressible Navier-Stokes equations in conserved variables and present a finite-volume-based discretization for the linearized equations. In Sec. III we construct the linear stability eigenvalue problem corresponding to the geometry and flow conditions corresponding to the experiment [7] conducted in the High SuperSonic Tunnel at the University of Manchester on a 12°-22° double wedge. We demonstrate the bifurcation of the two-dimensional steady-state flow to three-dimensionality via a global instability as the turn angle at the second ramp is gradually increased. The results from global linear stability analysis are corroborated with direct numerical simulations and a simplified physical mechanism of the instability is presented. In Sec. IV we compare the predictions from global linear stability with the experiment. Verification of the linearized equations is presented in the Appendix.

II. NUMERICAL METHODOLOGY FOR LINEAR ANALYSIS

We analyze the stability of the slender-double-wedge flow by investigating the associated small-perturbation dynamics. The governing equations for small perturbations are linear after terms involving higher powers of perturbation quantities are neglected.

Linear stability of compressible flows involves transport of two thermodynamic perturbation variables in addition to the flow perturbation variables. Previous global stability analyses linearize the governing equations in primitive variable sets such as (p, u_i, T) [29] and (p, u_i, s) [30] or the conserved variable set (p, u_i, E) [35]. We linearize the equations in the conserved variable set as its validity and accuracy in the presence of shocks has been studied in the past [44,45]. Also, compressible base flow calculations typically solve for the conserved variable set. Employing linearization in the conserved variables is therefore relevant. We construct a global linear stability solver that is fully unstructured and uses a finite-volume discretization for the linearized compressible Navier-Stokes equations. The unstructured methodology is expected to make global stability analysis of high-speed flows of complex geometry configurations more convenient.

Later, in Sec. II B, we discuss the specific discretization employed for the present work. Our methodology discretizes the linearized compressible Navier-Stokes equations. An alternate method is to linearize the discretized nonlinear equations as is done via numerical differentiation by Mack and Schmid [46], for example. The two methods have been compared by Hall *et al.* [47] for conserved variable perturbations.

A. Conserved-variable-based linearization

The compressible Navier-Stokes equations in the conservation form are

$$\frac{\partial \mathbf{U}}{\partial t} + \frac{\partial \mathbf{F}_j}{\partial x_j} + \frac{\partial \mathbf{F}_j^{\mathrm{v}}}{\partial x_j} = 0, \tag{1}$$

where $\mathbf{U}$ is the vector of conserved solution variables, $\mathbf{F}_j = \mathbf{F}_j(\mathbf{U})$ is the inviscid flux vector, and $\mathbf{F}_j^{\mathrm{v}}$ is the viscous flux vector:

$$\mathbf{U} = \begin{pmatrix} \rho \\ \rho u \\ \rho v \\ \rho w \\ E \end{pmatrix}, \quad \mathbf{F}_j = \begin{pmatrix} \rho u_j \\ \rho u u_j + p\delta_{1j} \\ \rho v u_j + p\delta_{2j} \\ \rho w u_j + p\delta_{3j} \\ (E+p)u_j \end{pmatrix}, \quad \mathbf{F}_j^v = \begin{pmatrix} 0 \\ \sigma_{1j} \\ \sigma_{2j} \\ \sigma_{3j} \\ \sigma_{ij}u_i + q_j \end{pmatrix}. \tag{2}$$

Here $E = E_{\mathrm{int}} + \rho u_k u_k/2$ is the total energy and E_{int} is the internal energy of the gas. The viscous momentum flux is $\sigma_{ij} = -\mu(S_{ij} - 2/3 S_{kk}\delta_{ij})$ and the molecular heat diffusion is $q_j = -\kappa \partial_j T$. In addition, S_{ij} is the strain rate tensor. The viscosity of air is computed using Sutherland's law of viscosity $\mu = \mu(T)$. Conductivity κ for air is evaluated corresponding to a Prandtl number $\mathrm{Pr} \simeq 0.72$. The conserved flow variables are decomposed into the base and small-fluctuation components $\mathbf{U} = \overline{\mathbf{U}} + \mathbf{U}'$ such that $\|\mathbf{U}'\| \ll \|\overline{\mathbf{U}}\|$. The prime denotes the perturbation quantities and the overbar denotes the base flow variables. The convective flux can be expanded using a Taylor series about $\overline{\mathbf{U}}$ as

$$\mathbf{F}_j(\mathbf{U}) = \mathbf{F}_j(\overline{\mathbf{U}}) + \left.\frac{\partial \mathbf{F}_j}{\partial \mathbf{U}}\right|_{\overline{\mathbf{U}}} \mathbf{U}' + O(\mathbf{U}'^2). \tag{3}$$

The viscous flux involves spatial gradients in the primitive variable set $\mathbf{V}^T = (\rho, u, v, w, T)$ and can be written in the form [48]

$$\mathbf{F}_j^v = \mathbf{M}_{jk} \frac{\partial}{\partial x_k} \mathbf{V} \tag{4}$$

and decomposed into the base-state viscous flux and perturbation flux as

$$\mathbf{F}_j^v(\mathbf{U}) = \mathbf{F}_j^v(\overline{\mathbf{U}}) + \overline{\mathbf{M}}_{jk} \frac{\partial}{\partial x_k} \mathbf{V}' + \overline{\mathbf{M}}_j^{VD} \mathbf{V}'. \tag{5}$$

The matrices $\mathbf{M}_{ij}$ contain the transport coefficients and can be found in the Appendix. We neglect the terms that consist of viscosity perturbation μ' due to perturbation in temperature. Including these terms increases the computational cost of factoring the sparse matrix, but as is observed from direct numerical simulations (DNSs) later in the paper, their contribution to the instability growth rate is negligible. For the freestream conditions considered in our study, we find from DNS that μ' terms are relevant only in the region of shock-shock interaction and are at least an order of magnitude smaller in the separation bubble and the boundary layer. The term $\overline{\mathbf{M}}_j^{VD}$ is a rank-1 tensor and arises from linearization of the viscous dissipation $\sigma_{ij}u_i$ term. Subtracting the governing equations for the base flow state $\overline{\mathbf{U}}$ from Eq. (1), we obtain the governing equations for small compressible

perturbation

$$\frac{\partial \mathbf{U}'}{\partial t} + \frac{\partial}{\partial x_j}\left(\bar{\mathbf{A}}_j + \bar{\mathbf{A}}_j^v\right)\mathbf{U}' = 0, \quad \bar{\mathbf{A}}_j = \left.\frac{\partial \mathbf{F}_j}{\partial \mathbf{U}}\right|_{\overline{\mathbf{U}}}, \quad \bar{\mathbf{A}}_j^v = \left(\overline{\mathbf{M}}_{jk}\frac{\partial}{\partial x_k} + \overline{\mathbf{M}}_j^{VD}\right)\overline{\mathbf{N}}. \tag{6}$$

Since perturbations are small, the conserved variable set $\mathbf{U}'$ and the primitive variable set $\mathbf{V}'$ can be linearly transformed. Here the matrix $\overline{\mathbf{N}}$ is the transformation matrix such that $\mathbf{V}' = \overline{\mathbf{N}}\mathbf{U}'$. The use of conserved perturbation variables results in a conserved form of linear governing equations.

B. Unstructured finite-volume discretization

The conserved form of linearized Navier-Stokes equations can be discretized spatially using a finite-volume framework. The semidiscrete form of Eq. (6) can be expressed as

$$\frac{\partial \mathbf{U}_c'}{\partial t} + \frac{1}{V_c}\sum_f \left[\left(\bar{\mathbf{A}}_j + \bar{\mathbf{A}}_j^v\right)S_j\mathbf{U}'\right]_f = 0, \tag{7}$$

where the subscript c refers to the cell and f refers to the face. Further, S_k is the face normal vector scaled with the face area. We apply the modified Steger-warming-type flux splitting [49] to the inviscid linearized flux

$$\bar{\mathbf{A}}_f\mathbf{U}_f' \approx \bar{\mathbf{A}}_f^+\mathbf{U}_{fL}' + \bar{\mathbf{A}}_f^-\mathbf{U}_{fR}' = \bar{\mathbf{A}}_f\frac{\mathbf{U}_{fL}' + \mathbf{U}_{fR}'}{2} + (\bar{\mathbf{A}}_f^+ - \bar{\mathbf{A}}_f^-)\frac{\mathbf{U}_{fL}' - \mathbf{U}_{fR}'}{2}, \tag{8}$$

where $\mathbf{U}_{fL}'$ and $\mathbf{U}_{fR}'$ indicate, respectively, the left and the right reconstructed conserved perturbation values at the face and $\bar{\mathbf{A}}_f = \bar{\mathbf{A}}_j S_j$ is evaluated using $(\overline{\mathbf{U}}_{fL} + \overline{\mathbf{U}}_{fR})/2$. Writing $(\bar{\mathbf{A}}_f^+ - \bar{\mathbf{A}}_f^-)$ as $|\bar{\mathbf{A}}|$, the dissipative portion of the linearized perturbation flux can be expressed as $|\bar{\mathbf{A}}|(\mathbf{U}_{fL}' - \mathbf{U}_{fR}')/2$ and on the lines of the low-dissipation flux methodology of Subbareddy and Candler [50], it may be selectively activated at shocks and contact discontinuities by convolving the expression with an appropriate sensor α. High-order polynomial interpolation for $\mathbf{U}_{fL}'$ and $\mathbf{U}_{fR}'$ using neighboring cell and gradient values may be used to increase the spatial order of accuracy [51].

While solving the compressible Navier-Stokes equations, second- and higher-order spatially accurate solutions require limiting in the nonsmooth regions to ensure the total-variation-diminishing (TVD) property of the solution. Although perturbation variables do not develop shocks, while propagating through the shock, the perturbation characteristics encounter a discontinuity in wave speed. Therefore, higher-order spatial discretization of the perturbation equations requires limiters. A one-dimensional analog is linear wave propagation in heterogeneous media, where the application of limiters results in nonoscillatory solution at the interface [52–54]. However, perturbations may be accurately propagated through a normal shock without the use of limiters, with violation of the TVD property. For example, a third-order upwind method predicts the transmission coefficient of an acoustic perturbation wave incident on a normal shock within 5% for an $M = 3$ normal shock (Fig. 24 in Appendix).

It must be noted that the approach followed in this work involves linearizing the governing equations and applying the limiters to the discretized linear equations as a numerical treatment for accurate solution. An alternate approach is linearization of the discretized compressible Navier-Stokes equations, which involves linearization of the limiters themselves. In this work we do not use limiters as we solve the temporal eigenproblem and do not numerically propagate perturbations in time. For the slender-double-wedge problem considered, the oblique shock angles are small and we find that the second-order symmetric inviscid perturbation flux ($\mathbf{U}_{fL}' = \mathbf{U}_L'$, $\mathbf{U}_{fR}' = \mathbf{U}_R'$, and $\alpha = 0$) suffices for obtaining physical solutions to the eigenproblem, without the use of limiters on the perturbation variables. Zero numerical dissipation also avoids damping the eigenvalues of the normal perturbation modes, ensuring physically accurate asymptotic temporal behavior.

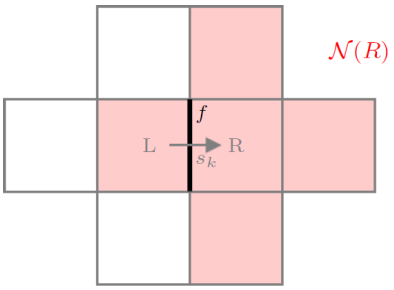

FIG. 1. Illustration of the 2D stencil for linearized viscous flux computation.

The gradient operator in the viscous Jacobian $\bar{\mathbf{A}}_j^v$ is evaluated using a deferred correction approach [55]. The cell center gradients are computed using weighted-least-squares methodology [56]

$$\left.\frac{\partial \phi}{\partial x_k}\right|_f = \frac{\partial \phi}{\partial x_j} s_j s_k + \frac{\partial \phi}{\partial x_k} - \frac{\partial \phi}{\partial x_j} s_j s_k \tag{9}$$

$$\approx d_R^{N(f)} \phi_R + d_L^{N(f)} \phi_L + \frac{1}{2}\left(\sum_{c \in \mathcal{N}(R)} d_c^{LS(R)} \phi_c + \sum_{c \in \mathcal{N}(L)} d_c^{LS(L)} \phi_c \right) = \sum_{c \in [\mathcal{N}(L) \cup \mathcal{N}(R)]} d_c^f \phi_c, \tag{10}$$

where ϕ is any physical quantity. As illustrated in Fig. 1 for a two-dimensional stencil, s_k denotes the face normal vector, L and R are the cells sharing f, and $\mathcal{N}(R)$ is the set of cells consisting of R and its immediate neighbors. The face gradient $\partial_k \phi|_f$ is expressed as a linear combination of the ϕ values in the cell stencil $\mathcal{N}(L) \cup \mathcal{N}(R)$ with the weight coefficient associated with cell c denoted by d_c^f. The coefficient $d_c[LS(e)]$ corresponds to the gradient at cell e evaluated using the weighted-least-squares method outlined by Shima *et al.* [56], while $d_c[N(f)]$ corresponds to the gradient at face f evaluated using ϕ_L and ϕ_R along the face normal s_k. This form of face gradient is consistent with the viscous flux used for base flow computation in the compressible finite-volume code US3D [57].

To compute spanwise periodic global eigenmodes, we seek perturbation solutions of the form

$$\mathbf{U}'(x, y, z, t) = \mathbf{U}'_{2D}(x, y) \exp[-i(\omega_r + i\omega_i)t + i2\pi z/\lambda_z], \tag{11}$$

where λ_z is the wavelength of the perturbation mode and ω_i is the growth rate. Substituting this perturbation form in the linear system of equations (7) results in a generalized eigenvalue problem for $\mathbf{U}'_{2D}$, which we solve using the shift-invert approach with the software PARPACK [58] and SuperLU [59].

III. BIFURCATION TO THREE-DIMENSIONALITY

In this section we study the global linear stability of the two-dimensional high-speed flow on a slender double wedge with respect to three-dimensional perturbations. A range of wedge turn angles is considered. For all interactions, the flow is globally stable to two-dimensional perturbations. In this case, constraining the DNS to remain two dimensions allows us to evaluate steady-state solution to the compressible Navier-Stokes equations. Beyond a certain turn angle, the two-dimensional steady-state solution is unstable with respect to three-dimensional perturbations. Using global stability analysis, we identify the critical turn angle at which the flow first supports an unstable mode. The spatial structure of the unstable mode is also obtained from the analysis. We verify this three-dimensional instability by carrying out three-dimensional direct numerical simulations.

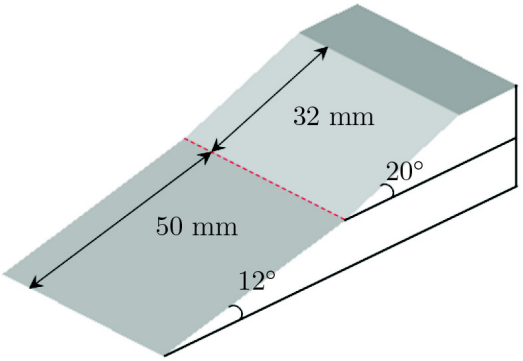

Freestream conditions

M_∞	5.0
U_∞	792.35 m/s
p_∞	1.22 kPa
T_∞	62.5 K
U_∞/ν_∞	13.6×10^6 m^{-1}

FIG. 2. Slender-double-wedge geometry and freestream conditions.

Further, we analyze the physical mechanism of the instability and demonstrate that streamwise deceleration of the separated flow plays an important role in the emergence of three-dimensionality.

A. Flow configuration and computational setup

The slender-double-wedge geometry we consider corresponds to the experiments of Yang *et al.* [7]. Figure 2 shows the geometry and the freestream conditions considered in this work.

The two-dimensional steady-state flow on the double wedge is computed using the finite-volume compressible flow solver US3D [57]. The second-order-accurate modified Steger-warming fluxes using MUSCL limiters are employed. The numerical method for computation of the base state has been validated with hypersonic double-wedge and double-cone experiments in the past [60]. The solutions are time marched to steady state implicitly using the method with Courant-Friedrichs-Lewy (CFL) number ramping. Since the enthalpy and temperature encountered in the flow field are low, we do not consider real gas effects in this study and consider a calorically perfect gas that follows the ideal gas law. An adiabatic wall boundary condition is imposed to match the conditions in the experiment where the test times last as long as 7 s. For a grid with 105 K cells, the streamwise grid resolution in the separation zone is 0.08 mm and the wall-normal transverse grid spacing in the shear layer region is approximately 0.04 mm. In the Appendix we show that this resolution is sufficient for global mode analysis. Increasing the resolution further has no appreciable effect on the resulting mode shapes or associated eigenfunctions.

Figure 3 shows the Mach contours and the recirculation bubble streamlines at the compression corner. The boundary layer separates 12.15 mm upstream of the corner, forming a separation shock. The δ_{99} thickness of the boundary layer at separation is $L = 1$ mm. The separated shear layer reattaches 11.4 mm downstream of the corner and is associated with a reattachment shock. The separation, corner, and reattachment points associated with the two-dimensional (2D)

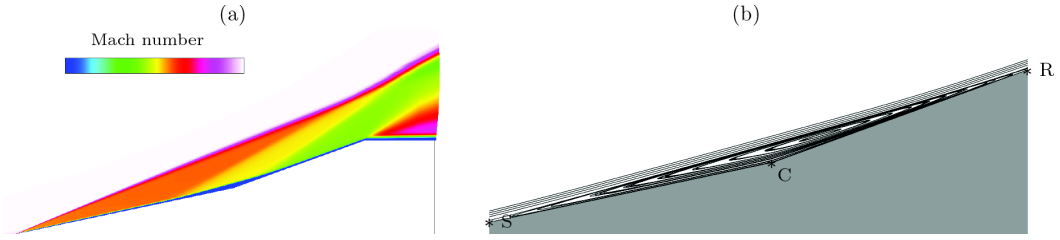

FIG. 3. (a) Mach number field on the 12°-20° slender double wedge at the freestream conditions mentioned in Fig. 2 and (b) 2D streamlines visualizing the recirculation region marked with the separation (S), corner (C), and reattachment (R) points.

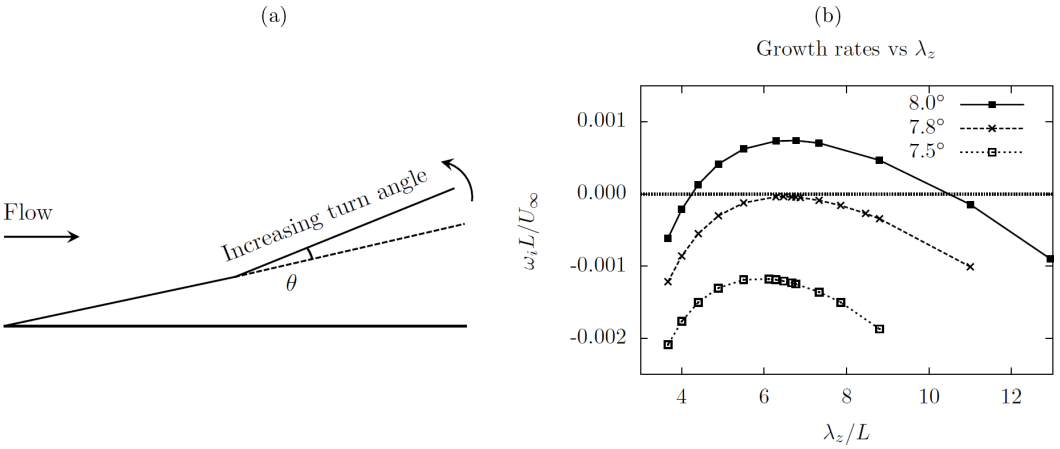

FIG. 4. (a) Schematic showing the variation of the turn angle via rotation of the second ramp about the compression corner and (b) associated bifurcation of the 2D steady flow on the slender double wedge.

steady-state flow field are marked as S, C, and R in the figures that follow. In the forthcoming sections, we will use the boundary-layer thickness at separation L as the reference length scale for nondimensionalization.

B. Global stability analysis

In order to investigate the onset of three-dimensionality, we evaluate the stability of the 2D flow to spanwise periodic perturbations of the form in Eq. (11). The spanwise wavelength of the perturbation is denoted by λ_z and the wave number is defined by $\beta = 2\pi/\lambda_z$. The resulting eigenvalue problem is solved for a set of the least stable eigenvalues ω. The imaginary part of the eigenvalue ω_i corresponds to the growth rate of the perturbation and the real part corresponds to the frequency.

We carry out stability analysis for several base flows at different turn angles at the same freestream conditions. As shown in Fig. 4(a), we vary the turn angle θ by rotating the second wedge about the corner point while the angle of the first wedge is held constant to approximately preserve the state of the boundary layer prior to separation. Increasing θ increases the strength of the recirculation.

The boundary conditions on the perturbations for linear stability analysis are implemented in the form of sponge zones upstream near the leading edge, downstream on the shoulder of the slender double wedge, and in the wall-normal direction near the freestream. The sponge zone is implemented using a blending function $\theta(x, y)$ that varies from 0 in the interior to 1 in the boundary sponge zones. The global matrix entry $\tilde{A}_{ij}$ is obtained from the sponge-free nondimensional system matrix A_{ij} as

$$\tilde{A}_{ij} = A_{ij}(1-\theta) + \frac{\theta\delta_{ij}}{\epsilon}, \quad \epsilon = 10^{-10}.$$

The function θ consists of a tanh-based sigmoid function of the type $\tanh[(x - x_0)/l_s]$ as an indicator of where the perturbations must decay to zero. In the present case, the left and the right boundary θ functions are centered at $x_0 = 3.5$ and 82.0 mm, respectively, with $l_s = 1$ mm. The modes reported in this study are found to be insensitive to the strength and location of the sponge, provided they are away from the recirculation region.

For the geometry and conditions considered in this study, we find that the least stable eigenvalue is three-dimensional and nonoscillatory, i.e., $\omega_r = 0$ and $\beta \neq 0$. Figure 5 shows the eigenvalue spectrum at $\lambda_z \sim 6.28$ for θ at 7.5° (black) and 8° (red). The spectra for the two turn angles show that an increase in θ increases the growth rate ω_i associated with the least stable mode and beyond the critical angle the 2D flow becomes unstable to 3D perturbations with $\omega_i > 0$.

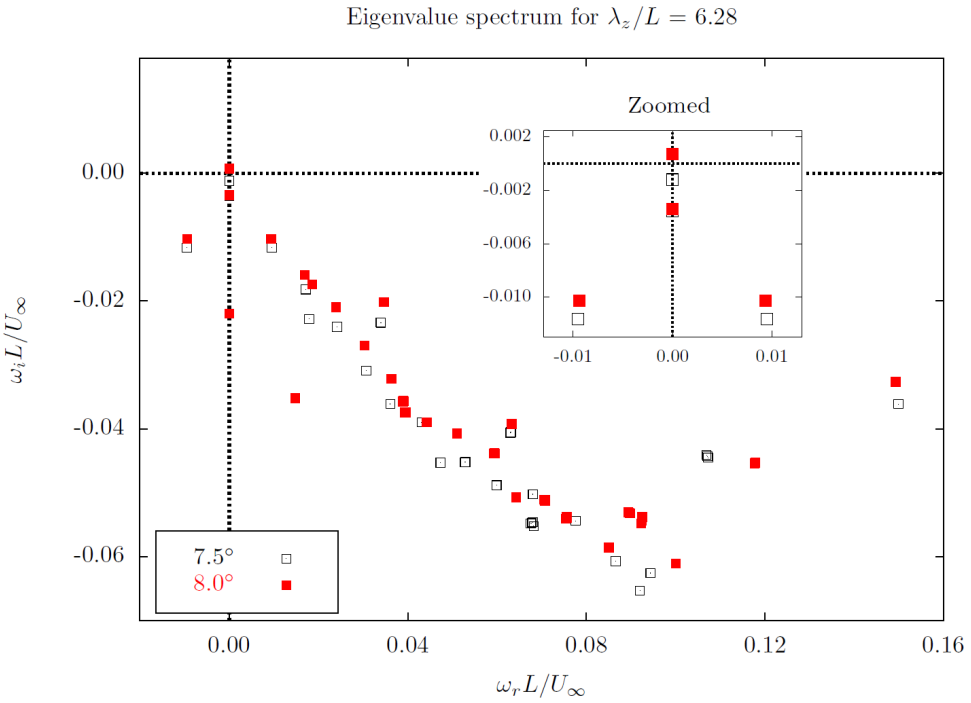

FIG. 5. Growth rate vs angular frequency: shift in the eigenvalue spectrum at the least stable λ_z with an increase in turn angle at bifurcation.

The analysis is repeated for different perturbation spanwise wavelengths λ_z and it is found that the growth rate ω_i peaks at a specific spanwise wavelength, selected by the base flow. With respect to perturbations with very large and vanishingly small wavelengths, the base flow is found to be stable for all turn angles (Fig. 4).

Figure 6 shows the 2D cross section of the perturbation variables corresponding to the most unstable eigenmode and the three-dimensional visualization of w' and T' isosurfaces. All the perturbation variables are real, except w', which is 90° out of phase and is purely imaginary. While the spanwise perturbation velocity is confined to the separation bubble, the perturbation in temperature is present well within the reattached region of the boundary layer. The pressure perturbation field exhibits periodicity in the streamwise direction with a wavelength that is approximately equal to the separation bubble length. We also note that the velocity perturbation components u' and v' are in phase with respect to spanwise variation. The pressure component in the upstream half of the separation bubble is 180° out of phase with u'. The w' component is 90° out of phase with u' and p'.

To illustrate the role of the three-dimensional instability on the topology of the recirculation, we superpose the unstable mode on the base flow with the three-dimensional velocity field obtained as $u_i = \bar{u}_i + \epsilon u_i'$. Here u_i' denotes the normalized perturbation velocity field and the parameter ϵ denotes the amplitude of the perturbation. The perturbation velocity field is normalized by the L^2 norm of the nondimensional perturbation vector. Freestream base-state values are used for nondimensionalization. The resulting three-dimensional flow field is therefore a function of the amplitude of the eigenmode imposed. Small amplitude causes a small deviation from the two-dimensional state but changes the flow topology. As shown in Fig. 7, the flow inside the recirculation bubble organizes into 3D cells of spanwise length $\lambda_z/2$. These cells are bounded in the spanwise direction by xy planes where $w = 0$. Because no flow can cross these planes, fluid elements belonging to a cell never leave it. Within a cell, however, fluid elements follow three-dimensional

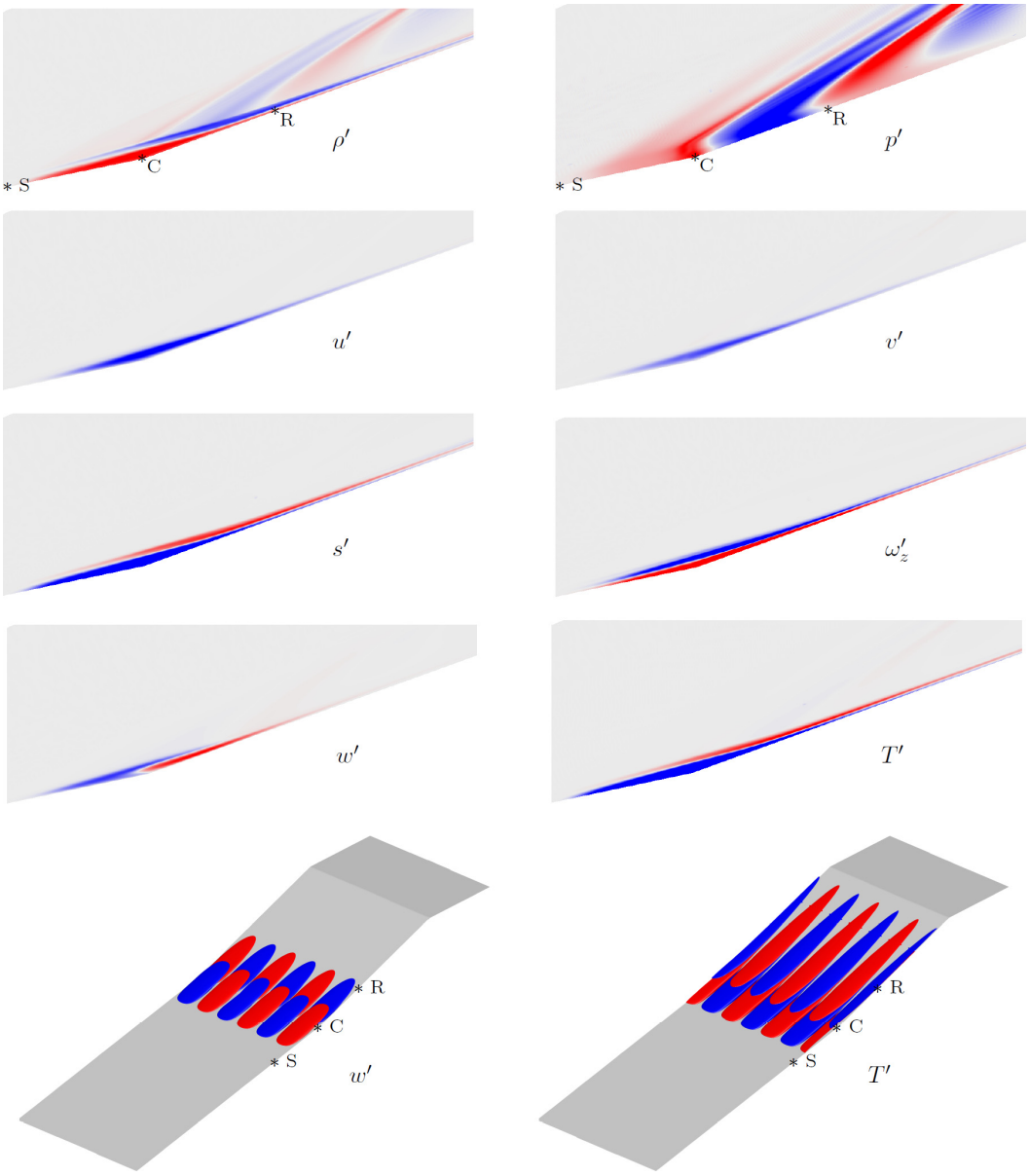

FIG. 6. Unstable eigenmode at $\lambda_z/L = 6.28$: 2D slices and 3D isosurfaces of different perturbation variables.

paths. One edge of each cell coincides with the spanwise location of maximum recirculation bubble strength, while the other edge coincides with the location of minimum recirculation strength. The cell pair repeats across the span.

To understand the three-dimensional flow within a cell, we consider the flow's critical points, in a manner similar to the analysis of Theofilis *et al.* [31]. In each xy plane, one critical point can be found at the center, or core of the recirculation bubble. A critical point in a plane is defined as the point where the in-plane velocity vector is zero. Because of the three-dimensional nature of the flow, this critical point can be a stable spiraling focus, an unstable spiraling focus, or a center. At the edge of the cell that corresponds to maximum recirculation strength, the core critical point is an unstable

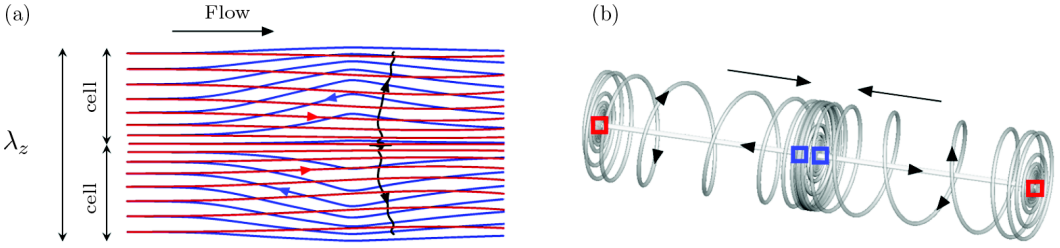

FIG. 7. (a) Topology of the 3D bubble reconstructed with $u_i = \bar{u}_i + \epsilon u_i'$, $\epsilon = 2$. The streamlines on the top are red ($u_i > 0$) and those at the bottom are blue ($u_i < 0$). (b) Simplified model of the 3D bubble structure with foci marked as squares (red denotes unstable and blue denotes stable).

focus, while at the opposite end of the cell, coinciding with minimum recirculation strength, the core critical point is of stable spiraling focus type. The flow expelled at the unstable focus spirals towards the stable focus along an outer corkscrew-type trajectory. Flow movement towards the stable focus is strongest at the outer periphery of the recirculation cell. As the outer flow approaches the plane of minimum recirculation, it is attracted back into the core. In the core, flow travels in span in the opposite direction, making the flow in the cell self-contained in the span. Figure 7(b) illustrates the topology of this three-dimensional flow pattern. In the core of the recirculation bubble, the flow from the stable focus to the unstable focus transports spanwise vorticity from regions of minimum to the regions of maximum recirculation, reinforcing the instability.

We can also understand the flow topology by considering no-slip critical points along the wall, as shown in Figs. 8(a)–8(c). In this view, the separation line is an attractor where streamlines from the oncoming flow meet those of the recirculating flow downstream. Conversely, the reattachment

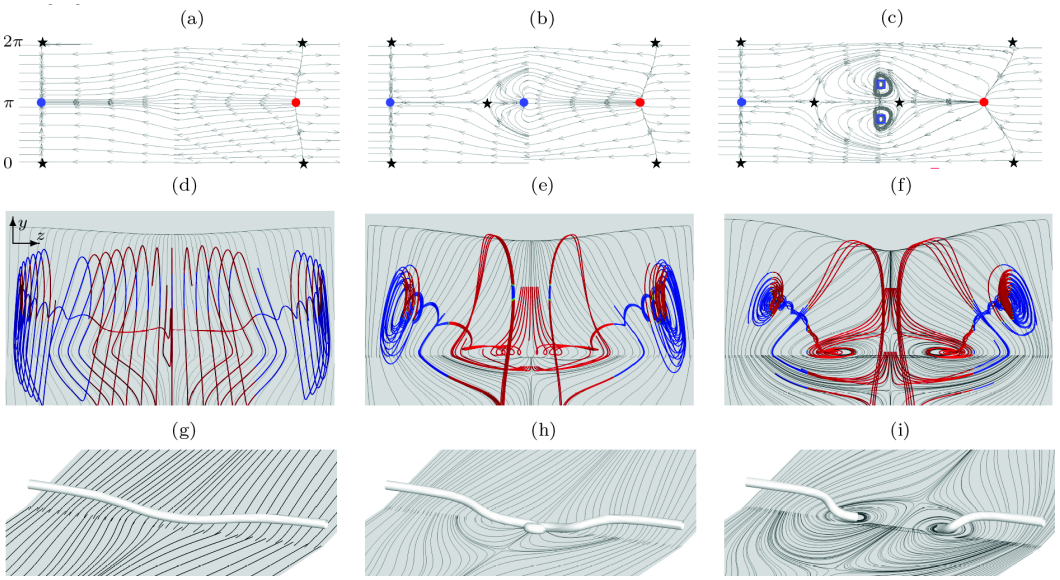

FIG. 8. The 3D bubble reconstructed with $u_i = \bar{u}_i + \epsilon u_i'$ with increasing mode amplitude $\epsilon = 5$ (left column), $\epsilon = 10$ (middle column), and $\epsilon = 20$ (right column): (a)–(c) critical points on the wall streamlines (circles denote nodes, stars denote saddle points, and squares denote foci; red denotes unstable and blue denotes stable), (d)–(f) volume streamlines colored with T' (red is positive and blue is negative), and (g)–(i) the vortex tube passing through the stable foci.

TABLE I. List of DNS runs for GLSA verification.

Run no.	θ	L_z (mm)	L_z/λ_z	Initial condition	Verification
1	8.0	14.0	2	$\overline{\mathbf{U}}_{2D}$	flow becomes three-dimensional
2	7.5	14.0	2	$\overline{\mathbf{U}}_{2D}$	flow remains two-dimensional
3	8.0	28.0	4	$\overline{\mathbf{U}}_{2D}$	λ_z with the highest growth rate
4	8.0	14.0	2	$\overline{\mathbf{U}}_{2D} + \epsilon\mathbf{U}'$	growth rate
5	8.0	7.0	1	$\overline{\mathbf{U}}_{2D} + \epsilon\mathbf{U}'$	wall streamline topology near nonlinear saturation

line is a repulsor where flow impinging on the wall splits and turns both upstream and downstream. The three-dimensional perturbation imparted by the global mode forms an alternating series of saddle and stable-node critical points along the separation line and a series of saddle and unstable-node critical points along the reattachment line. For the compression ramp, we observe that the stable nodes along the separation line align with the unstable nodes along the reattachment line downstream. This is the same pattern as that observed for incompressible separation bubbles [32], but is different from the pattern observed for oblique shock–boundary-layer interactions. In the latter case, the stable and unstable nodes were 180° out of phase [30].

As the amplitude of the perturbation is increased, although the basic structure of the 3D cell remains the same, the flow structure evolves. Increasing ϵ and its effect on critical points at the wall is shown in Figs. 8(a)–8(c). In addition to the critical points in the separation and reattachment lines, critical points appear within the separated flow region beyond a certain perturbation amplitude. The stable foci move closer to the wall with increasing ϵ and eventually attach to the wall. This may be understood physically by visualizing a straight vortex line along the z axis in the two-dimensional base flow. As can be seen in Figs. 8(g)–8(i), the vortex line develops spanwise undulations that grow as a result of the instability. Beyond a certain critical amplitude, the vortex line splits and attaches to the wall, connecting with its image. Also, Figs. 8(d)–8(f) show that T' is positive at the foci and negative away from them. The velocity field reconstructed with a large-amplitude perturbation ($\epsilon \gg 0$) reveals interesting flow features. The counterrotating streamlines on the wall are similar to those observed due to corner vortices in oblique shock–boundary-layer interaction with a turbulent incoming boundary layer [61]. Similarly, the spanwise tornadoes shown in Fig. 8(f) have been observed earlier via particle image velocimetry in the work of Dussauge *et al.* [62].

C. Direct numerical simulations

In this section, we use DNSs to verify the existence of the three-dimensional instability and dominant spanwise wavelength, independently of linear analysis, the growth rate of the linearly unstable eigenmode by introducing the mode obtained from GLSA into the DNS, and the appearance of late-time wall-streamline pattern as predicted from linear analysis. We use low-dissipation second-order spatially accurate kinetic-energy-consistent fluxes in the US3D hypersonic flow solver to perform DNS. Crank-Nicolson implicit time marching is employed with a CFL number of 5, which we found to be low enough such that lowering it yet further did not change the evolution of the three-dimensional perturbations. A 3D grid created by spanwise extrusion of the 2D grid used for the steady base flow calculations is used. Periodic boundary conditions are applied in the span. In all DNS runs, the spanwise resolution is fixed at 32 grid points per wavelength corresponding to the most unstable perturbation mode.

The set of DNS cases considered in this study are listed in Table I. As a first check, we first consider two DNSs (run 1 and run 2) corresponding to $\theta = 8.0°$ and 7.5°, respectively. According to global stability analysis, the former should remain stable to 3D perturbations while the latter should be unstable. While we do not initialize either simulation with three-dimensional perturbations, numerical round-off error provides an extremely-low-level three-dimensional forcing

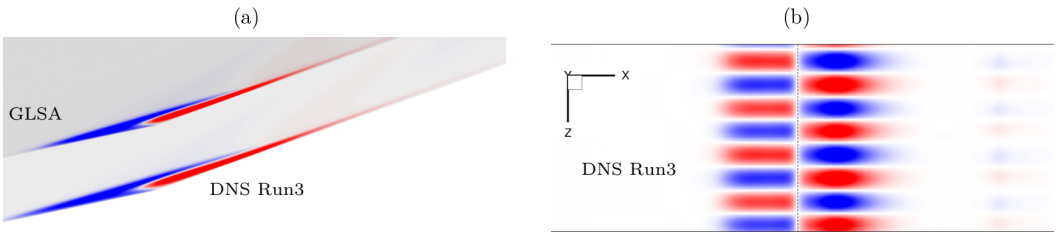

FIG. 9. Spanwise perturbation velocity w' in DNS run 3 at approximately $tU_\infty/L = 6000$ (a) on the z plane (GLSA mode overlaid for comparison) and (b) from the top view of near-wall planes.

in both cases. After running the simulation for a long time, we observe that three-dimensional flow structures emerge in the $\theta = 8^\circ$ flow, but the $\theta = 7.5^\circ$ run for the same amount of time remains two-dimensional. This confirms that the global stability analysis does indeed predict the onset of three-dimensionality in double-wedge flow and that DNS is consistent with the stability analysis.

Furthermore, we observe that the three-dimensional flow structures in the case of $\theta = 8^\circ$ have spanwise wavelength λ_z corresponding to the wavelength associated with the highest growth rate predicted from linear stability analysis [see Fig. 4(b)]. To check that this λ_z is independent of the spanwise length of the computational domain, we perform a third DNS (run 3) at $\theta = 8^\circ$ but with a computational domain having twice the spanwise width. This simulation resulted in structures having the same spanwise wavelength as the first simulation, run 1 [run 1 captured two spanwise wavelengths, while the simulation with the double spanwise domain captured four, as can be seen in Fig. 9(b)]. This demonstrates that, besides predicting the onset of three-dimensionality, the global stability analysis predicts the spanwise wavelength of the three-dimensional flow structures that emerge from the 2D flow.

Figure 9(a) shows a comparison of the mode shape predicted by global stability analysis and a slice through the three-dimensional flow that develops in run 1. The qualitative agreement is remarkable, indicating that global stability analysis accurately captures the essential flow physics of the predicted three-dimensional double-wedge instability. A quantitative comparison of the profiles is shown in Fig. 10. The w profiles in the figure are lifted and more amplified downstream in comparison to the linear stability results. This is not a surprising result. As the instability grows, it affects the upstream boundary layer and the separation shock, resulting in modifications to the nominally two-dimensional state. We must emphasize that Fig. 10 does not serve as a verification exercise for linear analysis.

To further verify the global stability results, we measure the growth rate of the three-dimensional perturbation in the DNS. We run the $\theta = 8^\circ$ case initialized with the linearly unstable global mode

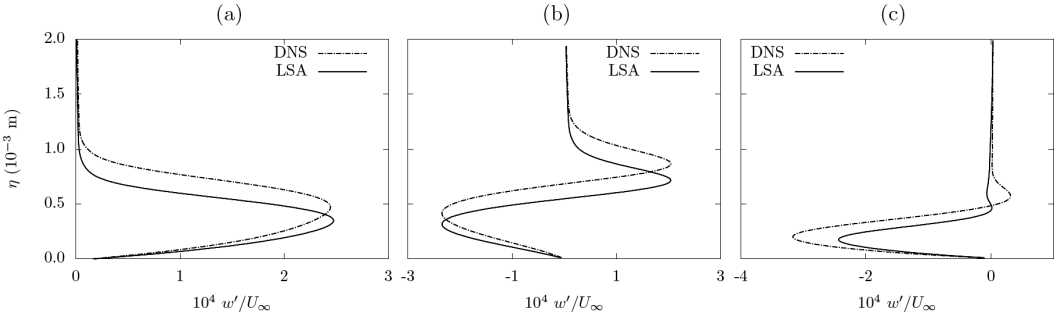

FIG. 10. Profiles of w from run 1 at late times compared with w' of the most unstable eigenmode of the 2D steady-state flow for (a) $\xi/L = 8$, (b) $\xi/L = 13$, and (c) $\xi/L = 18$.

overlaid on the base flow. To save computational resources, we choose a smaller spanwise domain width such that only one spanwise wavelength is contained within the domain. As can be seen in Fig. 11(a), after a brief transient, the perturbation grows exponentially at the rate predicted by the global stability analysis.

After a very long run time, the global mode in the DNS grows enough that the stable foci in the bubble core attach to the wall [Fig. 11(b)]. When this happens, we observe the foci to form in the wall streamlines just as predicted from global stability analysis (see Fig. 8). While the perturbation eventually undergoes nonlinear saturation in the DNS, it is interesting to note that the predictions of wall-streamline patterns obtained from linear analysis hold true even after timescales on the order of 400 flowthrough times. However, we do not simulate the three-dimensional flow field to its asymptotic state as the small growth rate of the instability results in large computational cost.

D. Physical mechanism of instability

In the previous sections we have demonstrated the presence and investigated the evolution of the three-dimensional instability using global linear stability analysis and direct numerical simulations. In this section we analyze the physical mechanism driving the instability. This is important because the least stable eigenmode is structurally similar, below and above the critical turn angle θ_c. However, while the mode decays at $\theta < \theta_c$, it is amplified for $\theta > \theta_c$. Specifically, we identify the imbalance in the modal dynamics that causes growth.

The transport equations for the perturbation quantities ρ', u_i', p', and T' can be written in the form

$$\overbrace{\frac{\partial \rho'}{\partial t} + \bar{u}_j \frac{\partial \rho'}{\partial x_j}}^{\text{Transport } \mathcal{T}} = \overbrace{-u_j' \frac{\partial \bar{\rho}}{\partial x_j}}^{\text{Production } \mathcal{P}} \overbrace{- \left(\rho \frac{\partial u_j}{\partial x_j}\right)'}^{\text{Linearized Lagrangian source } \mathcal{S}}, \tag{12}$$

$$\frac{\partial u_i'}{\partial t} + \bar{u}_j \frac{\partial u_i'}{\partial x_j} = -\frac{(\rho u_j)'}{\bar{\rho}} \frac{\partial \bar{u}_i}{\partial x_j} - \frac{1}{\bar{\rho}} \frac{\partial p'}{\partial x_i} + \frac{1}{\bar{\rho}} \frac{\partial \tau_{ij}'}{\partial x_j}, \tag{13}$$

$$\frac{\partial p'}{\partial t} + \bar{u}_j \frac{\partial p'}{\partial x_j} = -u_j' \frac{\partial \bar{p}}{\partial x_j} - \gamma \left(p \frac{\partial u_j}{\partial x_j}\right)' + (\gamma - 1)\left(\tau_{ij} \frac{\partial u_i}{\partial x_j} + \frac{\partial q_j}{\partial x_j}\right)', \tag{14}$$

$$\frac{\partial T'}{\partial t} + \bar{u}_j \frac{\partial T'}{\partial x_j} = -u_j' \frac{\partial \overline{T}}{\partial x_j} - (\gamma - 1)\left(T \frac{\partial u_j}{\partial x_j}\right)' + \frac{\gamma - 1}{\bar{\rho} c_V}\left(\tau_{ij} \frac{\partial u_i}{\partial x_j} + \frac{\partial q_j}{\partial x_j}\right)', \tag{15}$$

where we have categorized the terms into transport $\mathcal{T}$, source $\mathcal{S}$, production $\mathcal{P}$, and viscous $\mathcal{V}$ terms. The transport terms arise due to advection of the perturbation by the mean velocity. The production terms, which can be positive or negative, arise from the nonlinear advective term with u_i' acting on the mean flow gradients. The source terms correspond to the perturbation component of the inviscid material derivative of the perturbation. For example, in Eq. (12), the source term is $(-\rho \nabla \cdot u_i)'$ which when linearized, is $\rho' \nabla \cdot \bar{u}_i + \bar{\rho} \nabla \cdot u_i'$.

In general, any term in one of the four categories mentioned above can amplify or suppress the perturbation locally. If we quantify the perturbation at a point in space using an energy norm, each term may then be identified as an amplifier or a suppressor by its contribution to the energy norm. We choose the Chu energy norm E_{CE} [Eq. (16)] proposed in Ref. [63] to evaluate the contribution budget. The Chu energy norm ensures that the time evolution of perturbation energy norm is independent of term involving $p' \nabla \cdot u'$. This takes into account the kinetic-energy–thermal-energy exchange within the perturbation dynamics and avoids unphysical growth in perturbation energy

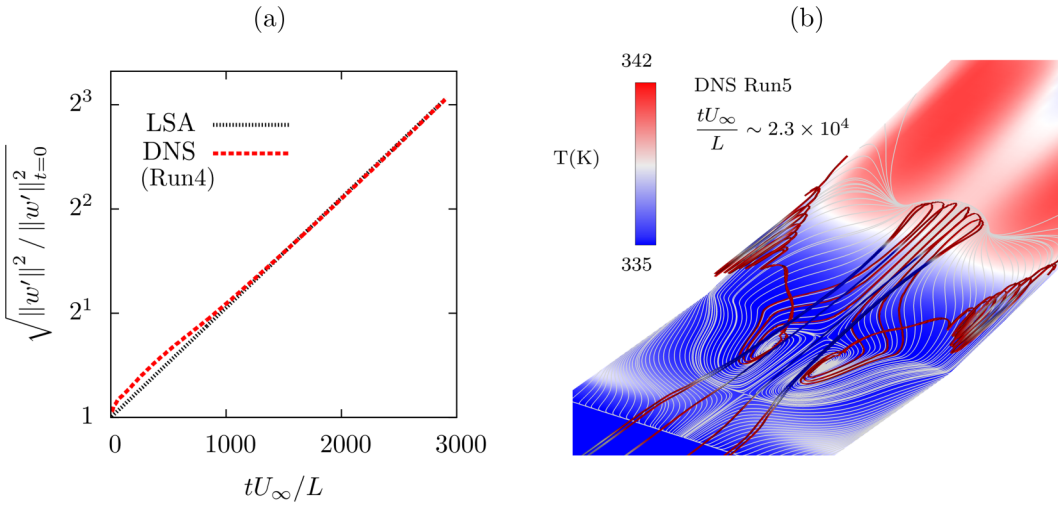

FIG. 11. (a) Comparison of the growth rate (for $\lambda_z/L = 6.28$) of the unstable eigenmode between DNS and global linear stability analysis and (b) appearance of foci on near-wall streamlines in the DNS flow field (for run 5 with $tU_\infty/L \sim 2.3 \times 10^4$). Near-wall streamlines are in white and volume streamlines and the wall are colored by temperature.

norm evolution [64]:

$$E_{\mathrm{CE}} = \frac{1}{2}\bar{\rho}u_i'u_i' + \frac{\bar{p}}{2}\left(\frac{\rho'}{\bar{\rho}}\right)^2 + \frac{\overline{E}_{\mathrm{int}}}{2}\left(\frac{T'}{\overline{T}}\right)^2, \tag{16}$$

$$\partial_t E_{\mathrm{CE}} + \mathcal{T} = \mathcal{P} + \mathcal{S} + \mathcal{V}, \tag{17}$$

where

$$\begin{aligned}
\mathcal{T} &= (\bar{p}/\bar{\rho}^2)(\rho'/2)\mathcal{T}_{\rho'} + \bar{\rho}(u_i'/2)\mathcal{T}_{u_i'} + (\overline{E}_{\mathrm{int}}/\bar{T}^2)(T'/2)\mathcal{T}_{T'},\\
\mathcal{P} &= (\bar{p}/\bar{\rho}^2)(\rho'/2)\mathcal{P}_{\rho'} + \bar{\rho}(u_i'/2)\mathcal{P}_{u_i'} + (\overline{E}_{\mathrm{int}}/\bar{T}^2)(T'/2)\mathcal{P}_{T'},\\
\mathcal{S} &= (\bar{p}/\bar{\rho}^2)(\rho'/2)\mathcal{S}_{\rho'} + \bar{\rho}(u_i'/2)\mathcal{S}_{u_i'} + (\overline{E}_{\mathrm{int}}/\bar{T}^2)(T'/2)\mathcal{S}_{T'}\\
&= -\partial_i(p'u_i') - \bar{p}\partial_i\bar{u}_i[(\rho'/\bar{\rho})^2 + (T'/\bar{T})^2],\\
\mathcal{V} &= \bar{\rho}(u_i'/2)\mathcal{V}_{u_i'} + (\overline{E}_{\mathrm{int}}/\bar{T}^2)(T'/2)\mathcal{V}_{T'}.
\end{aligned}$$

The terms that correspond to the four categories for the perturbation energy are obtained by contracting Eq. (13) with $\bar{\rho}u_i'$, Eq. (12) with $\bar{p}\rho'/\bar{\rho}^2$, and Eq. (15) with $\overline{E}_{\mathrm{int}}T'/\bar{T}^2$ and adding them together. This results in Eq. (17). It is important to note that the term categorization is dependent only on perturbation dynamics [Eqs. (12)–(15)] and not the definition of the perturbation energy norm [Eq. (16)]. For example, the transport term $\mathcal{T}$ for Chu's energy is different from $\bar{u}_j\partial_j E_{\mathrm{CE}}$. The norm chosen in this study therefore does not have any physical implications in the budget analysis other than the weighting of the different perturbation components.

To evaluate the contribution budget along the streamwise direction ξ, we integrate the term associated with each category in the wall-normal direction η. Here the 2D separation point marks $\xi = 0$ such that the streamwise coordinate values are $\xi/L \simeq 12$ at the compression corner and $\xi/L \simeq 24$ at the 2D reattachment point,

$$F(\partial_t E_{\mathrm{CE}}) = F(\xi) = \int_0^L \partial_t E_{\mathrm{CE}}(\xi, \eta)d\eta.$$

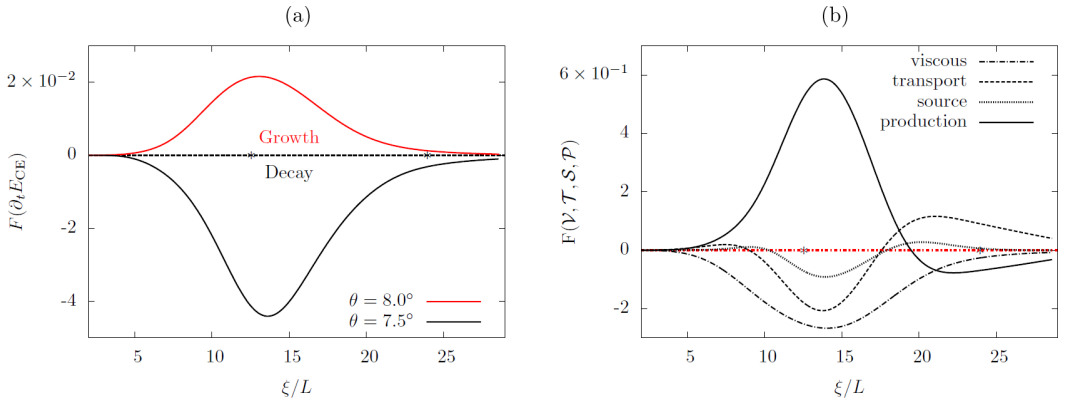

FIG. 12. (a) Wall-normal integrated rate of perturbation energy E_{CE} plotted along surface co-ordinate ξ for the stable and the unstable turn angle and (b) budget of contribution from individual terms $F(\partial_t E_{CE})$ for $\theta = 8°$; Bezier fits are plotted. Asterisks indicate the corner ($\xi/L = 12.2$) and base flow reattachment point ($\xi/L = 23.6$); the separation point $\xi/L = 0$ is outside the plot range.

Figure 12(a) shows the wall-normal integrated contribution F associated with the perturbation energy E_{CE}. The integrated amplification factor $F(\partial_t E_{CE})$ is negative for a stable wedge turn angle and is positive for an unstable turn angle.

The budget plot [Fig. 12(b)] shows that the production term dominates in the separation bubble, while the transport term is the dominant destabilizing term in the reattached boundary layer downstream of the bubble. The difference in the two angles is that the stronger interaction (larger turn angle) increases the magnitude of the contribution associated with each term. Past the critical turn angle, the amplifying terms surpass the suppressor terms in magnitude and the net result is that the perturbation mode is amplified in time. We should note that the production term is itself a sum of multiple terms involving streamwise and wall-normal velocities and derivatives. For example, within the production term for streamwise velocity perturbation energy $u'^2_\xi/2$, the amplification factor of $-u'^2_\xi \partial_\xi \bar{u}_\xi$ is the largest. Here u_ξ denotes the streamwise velocity component. In the discussion that follows, we will denote the local streamwise velocity component u_ξ by u and the local wall-normal velocity component u_η by v for readability.

The budget analysis provides us with information about how and where the perturbation mode is primarily amplified. We show that the driving mechanism behind the growth of the eigenmode can be traced to a local exponential instability. We begin by tracking the growth of spanwise velocity which causes flow three-dimensionality. By examining the magnitude of the terms in the spanwise velocity perturbation equations, we find that the term involving p' provides the largest amplification. Therefore, growth of w' is attributed to development of spanwise pressure peaks and valleys. Similarly, examining the evolution equation for p', we find that the peaks and valleys are produced by u' perturbations. However, the mechanism of p' amplification in the upstream half and the downstream half of the bubble is different. In the upstream half, pressure perturbations are amplified by u' acting against the mean adverse pressure gradient, while in the downstream half, dilatation of the perturbation $\nabla \cdot u'$ is the primary destabilizer. The largest term constituting $\nabla \cdot u'$ is $\partial_\xi u'$ involving streamwise velocity perturbation. After w' and p', we then scrutinize the terms in the u' equation. The production term $-u'\partial_\xi \bar{u}$ is found to be the primary amplifier term. Streamwise deceleration in the recirculating flow $\partial_\xi \bar{u} < 0$ results in local u' evolution of the form $\dot{u}' \sim ku'$, where k is a positive real number. This is an exponential growth equation.

Figure 13 shows that the base flow deceleration amplifies u' inside the recirculation bubble. The physical intuition behind this inviscid instability may be invoked from rapid distortion theory where compression of mean flow leads to growth of perturbations, while straining of the mean flow makes

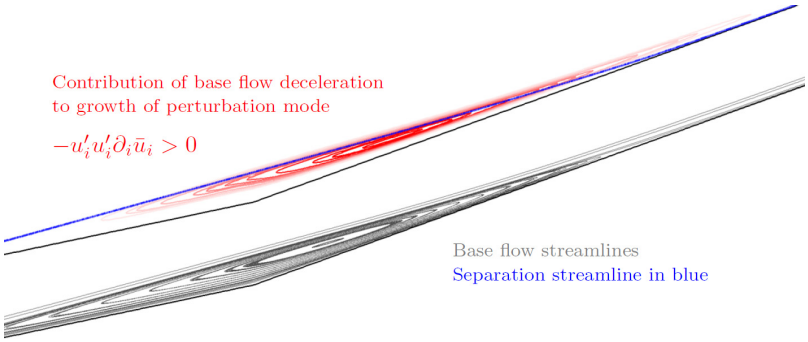

FIG. 13. Lines colored on a white-red scale mark the region where the contribution of the mean flow deceleration term to the perturbation energy is positive; mean flow streamlines are plotted in gray for comparison.

the perturbations decay. The dominant physical mechanism driving the growth of spanwise flow structures may therefore be described in the schematic shown in Fig. 14.

The η-z plots in Fig. 14 show one spanwise wavelength of the perturbation. The $w' = 0$ planes are seen to contain the two cells mentioned in Sec. III B. In the upstream half of the bubble, the spanwise movement of fluid in the bubble is towards the center (stable node at separation; see Fig. 8), while in the downstream half of the bubble, it is away from the center (unstable node at reattachment). We had earlier visualized the streamline topology associated with this perturbation field using blue colored streamlines in Fig. 7(a). As fluid moves from the high- to the low-pressure region, p' and w' can be seen to be 90° out of phase.

Previously, we traced the cause of growth in w' to growth in u'. Similarly, by following the dominant amplifying terms, we can identify the driver mechanism of T' streaks. Temperature perturbation is produced primarily by wall-normal velocity perturbation v' working against the base wall-normal temperature gradient $\partial_\eta \bar{T}$ in the reattaching shear layer. The primary amplifier term for v' is found be $u'\partial_\xi \bar{v}$. Separately, in the entirety of the bubble, $\nabla \cdot u'$ also amplifies T'. Therefore, like w', growth of T' is indirectly driven by u'.

Although we have postulated a simple local model for the physics that drives the exponential growth of the perturbation mode, the global nature of the instability involves all terms actively operating together, particularly the transport terms. The transport of perturbations and the global nature of the perturbation mode are physically synonymous.

E. Structural sensitivity

In the preceding section we identified the physical mechanism that drives the instability. Here we leverage the adjoint linearized Navier-Stokes equations to identify the regions in the flow where the unstable eigenmode is most sensitive to perturbations. The adjoint mode corresponding to the unstable mode (or the direct mode) corresponds to the perturbations that optimally initiate or external perturbation inputs that optimally trigger the unstable perturbation eigenmode in response [65]. We obtain the adjoint mode corresponding to the direct mode (perturbation eigenmode discussed in Sec. III B) by computing the adjoint eigenvalue problem associated with the discretized direct linear system (7). Figure 15(b) shows the adjoint mode corresponding to the spanwise momentum and is denoted by a plus sign superscript. The $(\rho w)^+$ mode may be contrasted with the $(\rho w)'$ component of the direct mode. While the direct mode is present primarily in the separation bubble and the reattached boundary layer, the adjoint mode is present in the upstream half of the separation bubble and all the way upstream in the incoming boundary layer. Physically, the modulus of the adjoint map in the plot represents the spatial region in which the linearly unstable direct

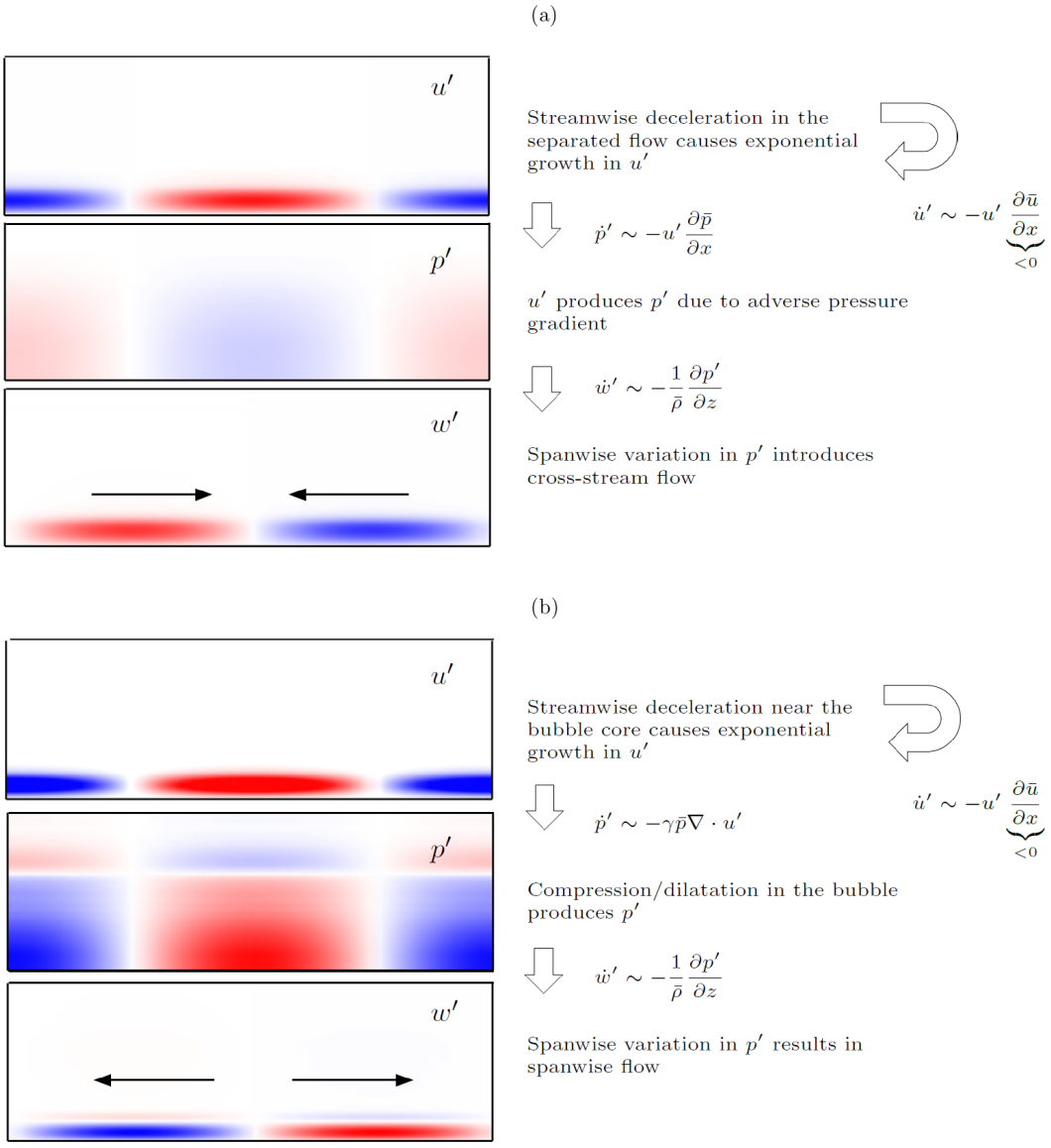

FIG. 14. Dominant mechanism of instability in the recirculation region: (a) mechanism in the upstream half of the bubble ($\xi/L = 8$) and (b) mechanism in the downstream half of the bubble ($\xi/L = 17$); $\hat{\xi}$ goes into the plane. The compression corner is at $\xi/L = 12$. The z axis is stretched by a factor of 1.5 for clarity of illustration.

mode is most receptive to external spanwise momentum forcing or the initial spanwise momentum perturbation.

In supersonic flow past compression corners, the presence of streamwise streaks near reattachment is often associated with Görtler-like vortices arising from centrifugal instabilities due to strong mean flow curvature. To understand whether the three-dimensional instability originates in the region of high streamline curvature, we compute a spatial sensitivity map of the eigenvalue ω of the direct mode using the method of Giannetti and Luchini [66]. The map helps locate the core of the three-dimensional instability by evaluating the strength of the local feedback of the unstable

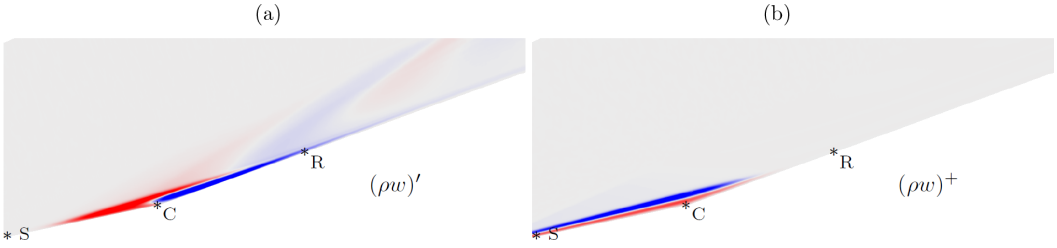

FIG. 15. (a) Direct mode corresponding to spanwise momentum perturbation and (b) the corresponding adjoint mode.

mode onto itself. The core therefore has high sensitivity as well as large perturbation response from the mode. At the core, a local modification to the structure of the global eigenvalue operator produces the greatest change in the eigenvalue or, equivalently, the growth rate of the eigenmode. For oscillator-type instabilities, the region is often referred to as the wave maker. The eigenvalue drift $|\delta\omega|$ caused by a spatially localized feedback of the form $\mathbf{f} = \delta(x_i - x_{i,0})\mathbf{U}$ can be shown [66] to be bound by the wave maker $\Lambda(x_{i,0})$,

$$\Lambda(x_i) = \frac{\|\mathbf{U}^+(x_i)\|\,\|\mathbf{U}'(x_i)\|}{\int_{\mathcal{V}} \mathbf{U}^+ \cdot \mathbf{U}' dV}. \tag{18}$$

Here $\mathbf{U}'$ and $\mathbf{U}^+$ correspond to the direct and the adjoint eigenmodes associated with the eigenvalue ω. Further, $\mathcal{V}$ is the domain and δ represents the Kronecker delta function. The instability mechanism resides in the region where the direct and the adjoint modes overlap and is strongest where Λ is maximum. The growth rate of the unstable eigenmode is most sensitive at that specific location to a change in the two-dimensional base flow. In the case of the current unstable mode, Fig. 16(a) shows that Λ peaks near the core of the separation bubble. Interestingly, this location coincides approximately with the location where production of E_{CE} peaks. The wave-maker analysis therefore establishes the instability mechanism at the core of the separation bubble.

Separately, we compute the Rayleigh coefficient Δ [Eq. (19)] and plot it alongside the eigenvalue sensitivity field Λ in Fig. 16 to compare the regions associated with centrifugal instability and the unstable global mode. A negative value of Δ is an inviscid criterion for the existence of short-wave centrifugal instabilities [67]. The Rayleigh discriminant is defined as

$$\Delta = 2\sqrt{u_i u_i}\,\omega_z/\mathcal{R}, \tag{19}$$

where $\mathcal{R}$ is the radius of curvature of the local streamline. The Rayleigh criterion is satisfied around the separation and reattachment regions, indicating that the wave maker associated with the global instability and the regions with $\Delta < 0$ are spatially decorrelated.

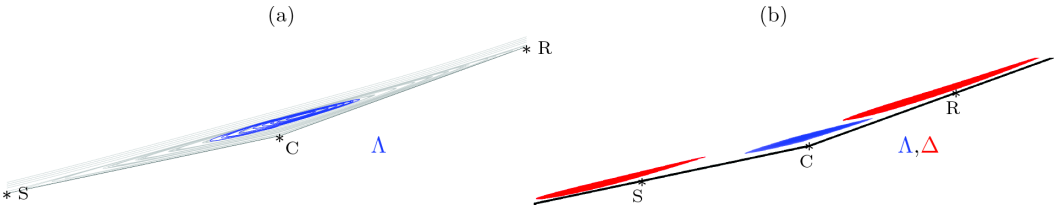

FIG. 16. (a) Contours of receptivity to spatially localized feedback λ in blue superimposed on the separation bubble streamlines (gray) and (b) regions with $\Delta < 0$ (red) plotted alongside the region with $\lambda > 0.1\lambda_{\max}$ in blue.

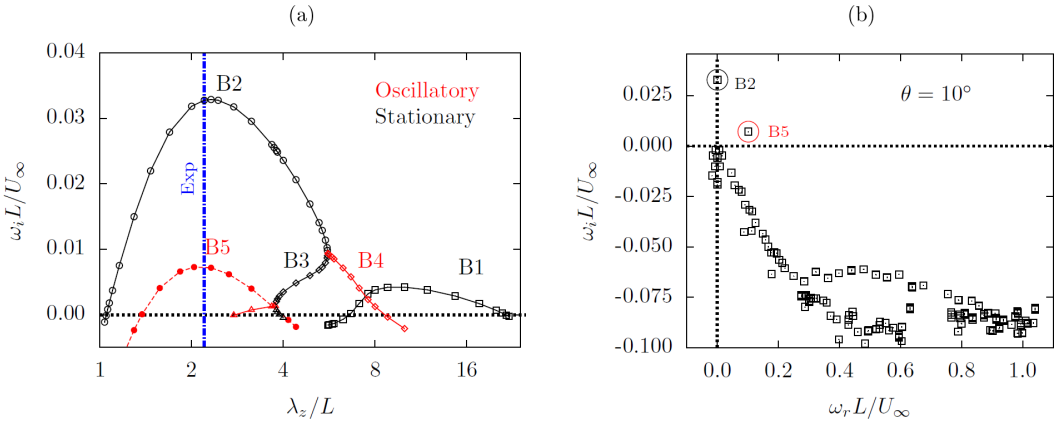

FIG. 17. (a) Growth rate of unstable perturbation modes vs spanwise wavelength λ_z for $\theta = 10°$ and (b) eigenvalue spectrum corresponding to the most unstable spanwise wavelength $\lambda_z/L = 2.3$ mm.

IV. COMPARISON TO EXPERIMENTAL OBSERVATIONS

Experimental visualization of wall temperature via temperature-sensitive paint measurements has been reported for the present geometry and freestream conditions at a turn angle $\theta = 10°$ in the work of Yang *et al.* [7]. The value of 10° is beyond the bifurcation point in the turn-angle parameter space. Nevertheless, we evaluate the global linear stability of the two-dimensional steady-state flow on this configuration to test the linear predictions against an experiment.

The validity of the two-dimensional steady flow on $\theta = 10°$ as a base state may be justified from an initial condition perspective. In the experiment, the flow sets up from rest $U_\infty = 0$ m/s to $U_\infty = 792$ m/s within a timescale on the order of milliseconds. Beyond the critical Re, when the flow becomes unstable to three-dimensional perturbations, the experimental flow does not move towards

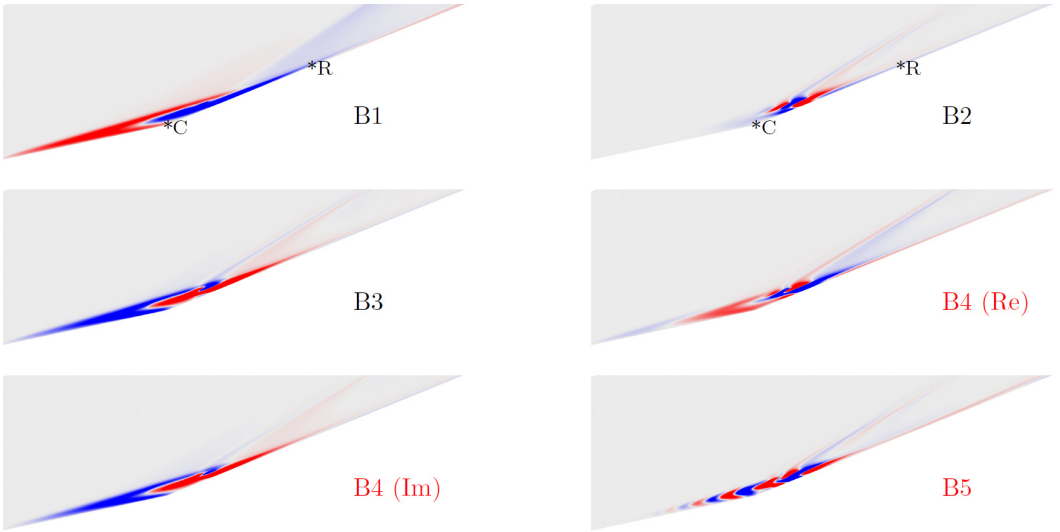

FIG. 18. Spanwise component of the perturbation velocity w' for different unstable mode branches identified in Fig. 17 with blue denoting negative and red denoting positive values. Here (Re) and (Im) refer to real and imaginary components, respectively. The w' fields correspond to normalized eigenvectors of the nondimensional linear system.

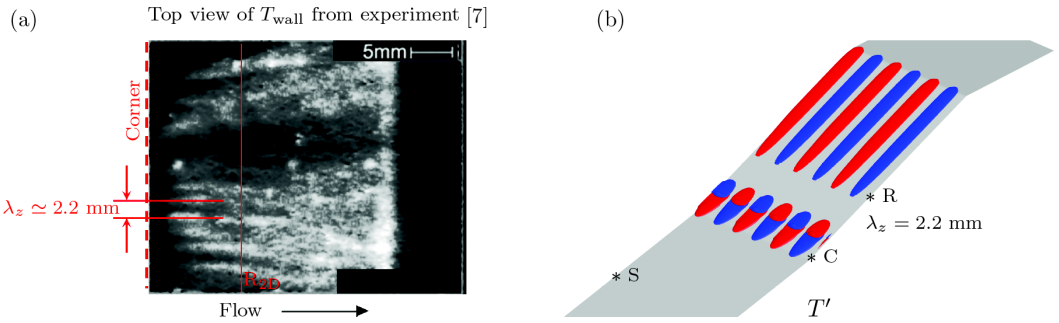

FIG. 19. (a) Streaks in wall temperature on the second ramp and (b) isosurface of temperature perturbation corresponding to the unstable eigenmode at $\lambda_z/L = 2.2$ for $\theta = 10^\circ$. The reattachment point corresponds to the 2D steady-state solution with adiabatic wall boundary conditions. The scales along the horizontal and vertical directions in (a) are the same [7].

the equilibrium three-dimensional flow state and then onward as would be the case in numerical continuation. Before the three-dimensional instability of the marginally unstable 2D steady flow sets in, the freestream velocity increases. Therefore, if the flow that initially sets up in the experiment is the 2D steady state, the associated three-dimensional instabilities can be physically relevant.

Figure 17(a) shows the unstable modes obtained for $\theta = 10^\circ$ on a ω_i-λ_z plot. The two-dimensional steady-state flow is stable to two-dimensional perturbations. Here the nondimensional length scale $L = 0.001$ m is kept unchanged from previous sections for consistency but does not represent the base flow boundary-layer thickness at separation for $\theta = 10^\circ$. In contrast to the $\theta = 8^\circ$ case, several unstable modes are obtained, including unsteady modes (shown in red). The modes are tracked by the spatial signature of the eigenvector and are divided into several mode branches. The most unstable mode is a stationary mode, similar to the 8° case, albeit with a smaller wavelength than in the 8° case. Investigation of the spatial map of the eigenvector reveals that this mode is structurally different from the mode that was most unstable at the bifurcation angle. We refer to this new mode branch as B2, while the mode branch that destabilizes the flow at 8° is labeled as B1.

Figure 18 shows the w' component associated with the different mode branches. The difference in B2 and B1 is clearly observed. In B2, w' is localized near the core of the separation bubble, slightly downstream of the corner, whereas in B1, w' is present in the entirety of the separation bubble. The wavelength from the experimental temperature-sensitive paint (TSP) visualization can be seen to compare well with the most unstable wavelength predicted by global linear stability analysis. This

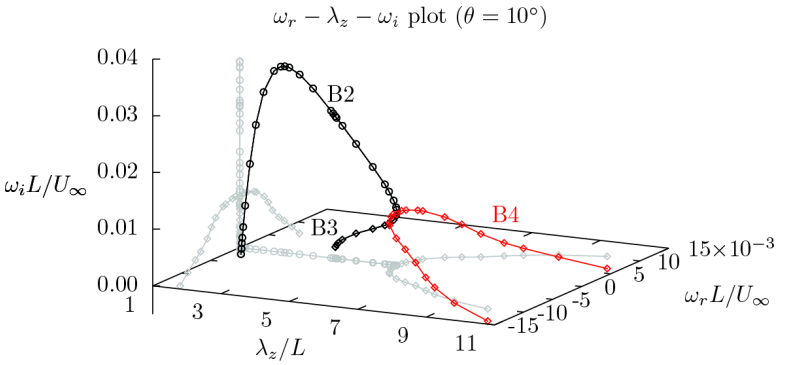

FIG. 20. Loci of the eigenvalues in the growth-rate–frequency–spanwise wavelength space. Projections on the ω_i-ω_r and λ_z-ω_r planes are shown in gray.

makes the unstable stationary global mode B2, a potential source of streamwise wall temperature streaks observed in the experiment. The T' isosurface associated with B2 is plotted next to the TSP images from the experiment for comparison (Fig. 19).

In addition to the stationary branches, two unstable oscillatory mode types, B4 and B5, are observed [shown in red in Fig. 17(a)]. Branch B4 forks into B3 and B2 as the wavelength λ_z is decreased. In the eigenvalue plane ω_i-ω_r, the two conjugate eigenvalues associated with B4 come closer to the $\omega_i = 0$ axis, merge (at the junction), and then move away from each other along the $\omega_i = 0$ axis, forming B2 and B3, respectively. Figure 20 helps visualize this movement in the ω_r-λ_z-ω_i three-dimensional space. The angular frequency ω_r associated with the mode B4 changes with perturbation wavelength λ_z. The real and the imaginary part of the B4 eigenmode in Fig. 18 are found to resemble the steady mode branches B2 and B3, respectively, indicating that the unsteadiness is associated with the perturbation oscillating between the two stationary instabilities.

The oscillatory mode B5, in contrast to B4, has a constant angular frequency independent of λ_z with the nondimensional value $\omega_r = 0.1$. The eigenvalue is identified in the spectrum in Fig. 17(b). The real part of the w' component (Fig. 18) exhibits streamwise periodicity in the upstream half of the separation bubble, an indication of traveling spanwise oblique perturbations that are associated with the temporal oscillations.

The purpose of global stability analysis at $\theta = 10^\circ$ in this paper is to establish physical relevance of the most unstable mode computed using the linearized flow dynamics. The spanwise wavelength of late-time wall temperature variation in the experiment is found to be similar to the most unstable wavelength predicted by the asymptotic stability analysis. The mode branches uncovered in this process require further analysis to understand the three-dimensionality and unsteadiness in high-speed flow on double wedges. The analysis of instabilities at larger turn angles is beyond the scope of the present work.

V. CONCLUSION

Mach 5 flow on a 12°-20° double wedge was shown to be intrinsically three-dimensional in the absence of upstream perturbations. The three-dimensionality in the flow was shown to arise from a linear instability of the two-dimensional recirculation bubble. As a consequence of the resulting three-dimensional recirculation, a streamwise streak pattern in wall temperature was observed. The streaks begin near the reattachment region and persist downstream on the second ramp, similar to those observed in experiments. More specifically, prediction of the streak spanwise wavelength from linear analysis was found to compare well with the wavelength deduced from temperature-sensitive paint images on a 12°-22° double-wedge experiment. The current results provide an explanation for the origin of streaks in addition to the centrifugal instability in the vicinity of flow reattachment. It is not clear which mechanism operates when or whether both mechanisms can operate together. However, our analysis shows that in the absence of external disturbances, the three-dimensionality in the separation bubble results in the longitudinal heat flux streaks.

A global analysis which evaluates stability with respect to spanwise periodic small perturbations was considered to investigate the three-dimensional linear instability of the two-dimensional steady-state double-wedge flow. Equations for small perturbations in conserved variables were discretized using a second-order spatially accurate finite-volume scheme. The temporal eigenvalue problem resulting from the linear system of equations for the base flow was then solved to assess its asymptotic stability. We started with a 12°-12° double wedge with no recirculation and gradually increased the turn angle at the second ramp by rotating it about the compression corner. The recirculation region increased in strength and at the 12°-20° double wedge the flow became unstable to three-dimensional perturbations. Direct numerical simulation of the flow on this geometry confirms the instability and presence of three-dimensional recirculation.

The dominant destabilizing mechanism on a 12°-20° double wedge was identified by analyzing the spatial fields of the individual terms in the unstable eigenmode dynamics. The analysis reveals that the mean gradients are responsible for the growth of the perturbation in the separation bubble,

while growth in the reattached boundary layer arises from downstream convection from the bubble. The exponential growth of the globally unstable mode is traced to an inviscid local instability in which streamwise deceleration of the two-dimensional flow results in exponential growth of streamwise velocity perturbation. Spanwise undulation of the streamwise velocity perturbation results in a pressure perturbation peak and valley in the span driving three-dimensionality. By identifying the wave maker or region where the instability exhibits highest sensitivity, we confirmed independently that the instability core lies in the separation bubble and not in the separation or reattachment regions, which can potentially host centrifugal instabilities.

Separately, beyond bifurcation, linear stability of the steady-state flow on a 12°-22° double wedge reveals several unstable mode families. The most unstable mode is a three-dimensional stationary mode, the wavelength of which is close to that of experimentally observed wall temperature streaks. Interestingly, this mode is distinct from the unstable mode observed on the 12°-22° geometry. While the role of perturbation modes at this turn angle requires further detailed analysis, the results give credence to the physical importance of three-dimensional instabilities in the recirculation region. Additionally, the presence of unstable low-frequency oscillatory modes can also provide insight into unsteadiness in shock-wave–boundary-layer interaction. Improved understanding of three-dimensional structures in high-speed laminar compression-corner flow can contribute towards transition prediction on technologically relevant geometries.

ACKNOWLEDGMENTS

We acknowledge support from the Office of Naval Research (Grant No. N00014-15-1-2522). We thank John Thome for help with the grids and Anthony Knutson for careful reading of the equations.

APPENDIX

1. Viscous flux matrices

In Sec. II the viscous flux is written in the form $\mathbf{F}_j^v = \mathbf{M}_{jk}\frac{\partial}{\partial x_k}\mathbf{V}$. The viscous flux matrices $\mathbf{M}_{ij}$ have entries that contain the velocity components u_i and transport coefficients μ, λ, and κ and can be written in the form

$$\mathbf{M}_{ij} = -\begin{bmatrix} 0 & 0 & 0 & 0 & 0 \\ 0 & a_{11} & a_{12} & a_{13} & 0 \\ 0 & a_{21} & a_{22} & a_{23} & 0 \\ 0 & a_{31} & a_{32} & a_{33} & 0 \\ 0 & b_1 & b_2 & b_3 & \kappa\delta_{ij} \end{bmatrix}, \tag{A1}$$

TABLE II. Comparison of the eigenvalues (ω_i, ω_r) with the reference values from the literature.

Shear layer			
	Eigenmode	Reference	Current method
	1[a]	(0.127,0.000)	(0.127,0.000)
	2	(−0.040, 0.396)	(−0.040, 0.396)
	3[b]	(−0.028, 1.479)	(−0.029, 1.476)
Boundary layer			
M_∞	(α, β)	Reference	Current method
0.5	(0.1,0.0)	(0.0022,0.0291)	(0.0022,0.0289)
2.5	(0.06,0.1)	(0.0006,0.0367)	(0.0005,0.0361)
1.0	(0.1,0.1)	(0.0013,0.0380)	(0.0008,0.0395)
6.0	(0.08,0.08)	(0.0010,0.0724)	(0.0007,0.0705)

[a]Corresponds to the shear mode.
[b]Corresponds to the acoustic mode.

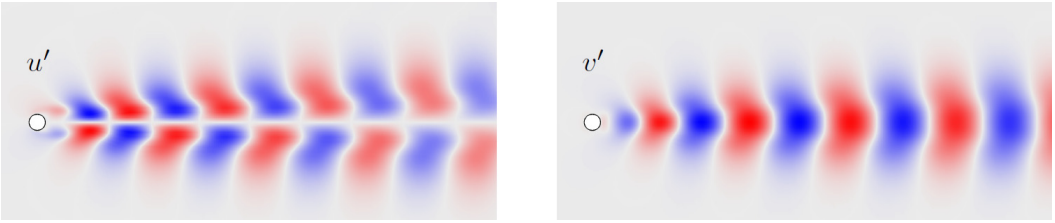

FIG. 21. Linearly unstable global mode for $\mathrm{Re}_D = 60$ and $M = 0.1$ flow past a circular cylinder.

where $a_{mn} = \mu(\delta_{ij}\delta_{mn} + \delta_{in}\delta_{jm}) + \lambda\delta_{im}\delta_{jn}$ and $b_n = u_m a_{mn}$. The matrix $\overline{\mathbf{M}}_j^{VD}$ that appears in the linearized viscous flux is

$$\overline{\mathbf{M}}_j^{VD} = \begin{bmatrix} 0 & 0 & 0 & 0 & 0 \\ 0 & 0 & 0 & 0 & 0 \\ 0 & 0 & 0 & 0 & 0 \\ 0 & 0 & 0 & 0 & 0 \\ 0 & \bar{\sigma}_{1j} & \bar{\sigma}_{2j} & \bar{\sigma}_{3j} & 0 \end{bmatrix}. \tag{A2}$$

2. Verification of linear system

We compare unstable eigenvalues of the 1D compressible flow temporal stability problem with the values from the literature. The reference values for the compressible shear layer with $M_\infty = 0.5$, vorticity thickness $\delta = 0.1$, and $\mathrm{Re}_\delta = 1000$ are taken from Mack and Schmid [46]. The corresponding eigenvalues obtained using the present formulation are reported in Table II. The reference values for compressible boundary-layer cases are taken from Malik [68] and Theofilis and Colonius [69]. The results at various Mach numbers and different streamwise-spanwise wave numbers (α and β) are shown in Table II. Slight discrepancies in the values for $M_\infty = 1.0$ and 6.0 are observed due to different viscosity and gas properties used for the base flow profiles in the reference.

Next we move to a 2D problem and compute the linearly unstable eigenmode for subsonic flow past a cylinder of diameter D. The eigenmode for the case $\mathrm{Re}_D = 60$ is shown in Fig. 21. At this Re, the cylinder wake is unstable and results in vortex shedding. The nondimensional eigenvalues for this particular case are found to be $\omega_i = 0.05$ and $\omega_r = 0.76$, which compare closely with those reported in the literature [70].

For verification with linear stability analysis of 2D laminar shock–boundary-layer interaction, we investigate the impinging oblique shock configuration at $M = 5.92$ [30]. The most unstable eigenmode is obtained for $\beta = 0.25$ with $\omega_i/2\pi = 3.1 \times 10^{-5}$. This is close to the value of $\omega_i/2\pi = 3.6 \times 10^{-5}$ obtained in Ref. [30]. The two-dimensional steady base flow and the spanwise velocity component of the most unstable perturbation eigenmode are plotted in Fig. 22.

Additionally, we also report the most unstable eigenmode obtained for an impinging oblique shock configuration at $M = 2.15$ [29]. At an impingement angle of 33°, the flow is predicted

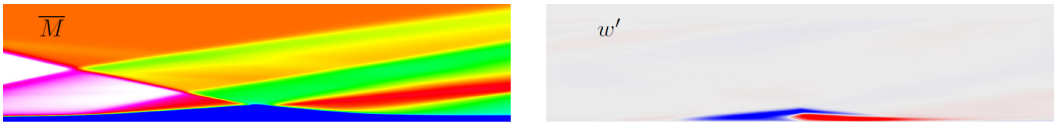

FIG. 22. Least stable global mode with wave number $\beta = 0.25$ obtained for oblique shock–boundary-layer interaction at $M = 5.92$ [30].

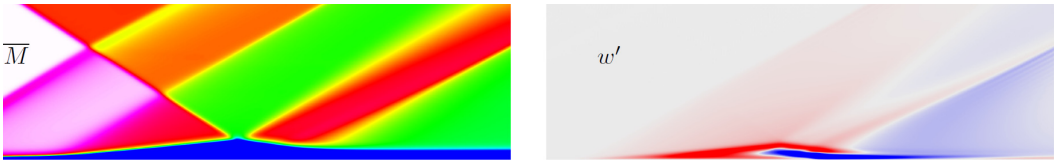

FIG. 23. Least stable global mode with wave number $\beta L_{\text{sep}} = 0.8$ obtained for oblique shock–boundary-layer interaction at $M = 2.15$ [29].

to be unstable in Ref. [29], with the spanwise wavelength of the dominant mode being 0.8, when nondimensionalized by the freestream velocity and separation length. We obtain an unstable stationary (zero-frequency) perturbation eigenmode at that wave number with a nondimensionalized growth rate of 0.12. However, this value is not consistent with the growth rate reported in Ref. [29]. The discrepancy is most likely due to inadequate grid resolution in Ref. [29] (5 K points) compared to 140 K cells used for the present study. The two-dimensional steady base flow and the spanwise velocity component of the most unstable perturbation eigenmode for this case are plotted in Fig. 23.

The discretized linear system for small perturbation in the presence of shocks is also investigated (Fig. 24). The transmission coefficient of planar acoustic perturbations interacting with a normal shock are compared with the analytical result [71]. A second-order symmetric scheme does not work in this problem as it involves numerical time integration. We therefore use a third-order upwind method for spatial discretization and a strong-stability-preserving Runge-Kutta method SSPRK2 for time marching the discretized linear equations. Note that no limiters are employed. The results compare fairly for normal shocks up to Mach 3.

3. Grid refinement

A grid refinement study is carried out for the eigenvalues presented in the paper. For each grid, a different base flow is computed and the corresponding global eigenvalue problem is solved. This is more strict than a grid refinement study of the eigenvalue problem with a base flow at fixed resolution. The normalized velocity and temperature profiles for $\theta = 8^\circ$ base flow are plotted in Fig. 25. The values for $\max(-u)/u_{\text{edge}}$ and $\max(-\rho u)/\rho u_{\text{edge}}$ at $\theta = 8^\circ$ are 0.108 and 0.036, respectively. The figure shows profiles of fields on three grids with increasing sizes $N = 105$, 155,

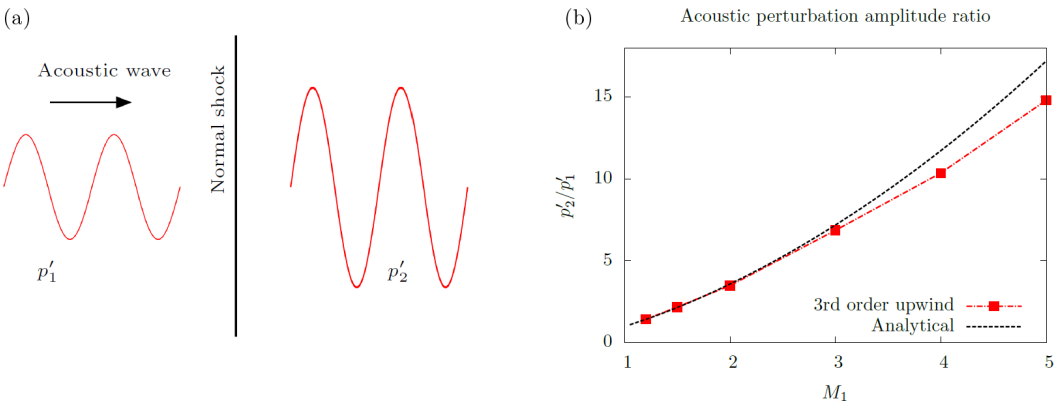

FIG. 24. (a) Schematic of the acoustic perturbation–normal shock interaction and (b) comparison of analytical transmission coefficient with that computed using third-order upwind discretization of linearized Euler equations in conserved variables.

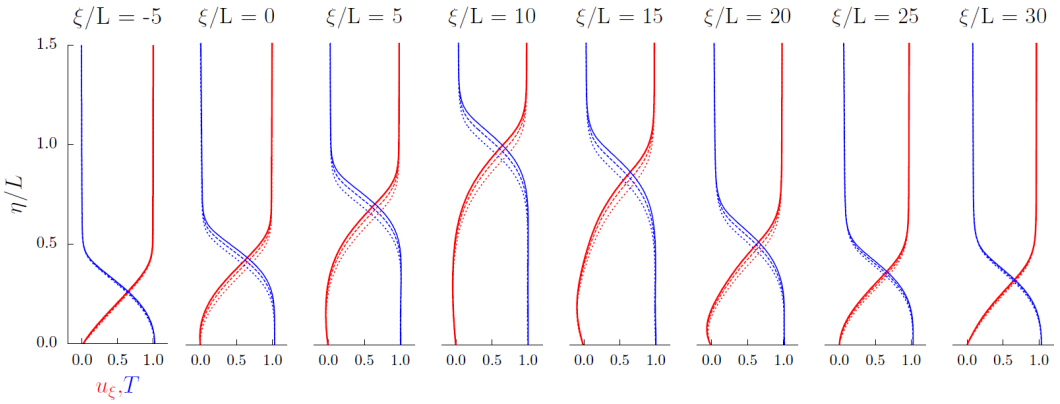

FIG. 25. Nondimensional velocity (red) and temperature profiles (blue) on three grids of increasing resolution (dotted line, 105 K; dashed line, 155 K; and solid line, 185 K); ξ is the coordinate along the surface with $\xi = 0$ at separation.

and 185 K cells. We find that the length of the recirculation bubble does not vary with increasing grid resolution. The maximum difference between the velocities predicted by the finest grids is within 10% at the compression corner, $\xi/L = 10$. The quantity of interest, i.e., the growth rate corresponding to the most unstable spanwise wavelength λ_z is grid converged (Fig. 26) for both cases $\theta = 8^\circ$ and 10°.

In the $\theta = 8^\circ$ case, we evaluate two methods of increasing the grid resolution: increasing streamwise ξ and wall-normal η resolution simultaneously and increasing the streamwise ξ resolution only, at a fixed wall-normal η resolution. The base grid size is $N = 105$ K grid cells. The $N = 105$ K grid has 200 points in the wall-normal direction, with $\Delta\eta = 2$ μm at the wall and $\Delta\eta = 1$ mm in the freestream. Consider Fig. 26(a). The $N = 57$ and 165 K grids correspond to simultaneous change in ξ and η resolution by a factor of 1.25. Separately, the $N = 80$, 155, and 185 K grids demonstrate the sensitivity of the eigenvalues to the streamwise spacing at a fixed wall-normal resolution. We note that with increasing grid resolution, the most unstable eigenvalue can increase or decrease depending on λ_z. Perception of an unusual trend where eigenvalues of high-spanwise-wave-number modes converge faster than low-wave-number modes is merely a consequence of this result.

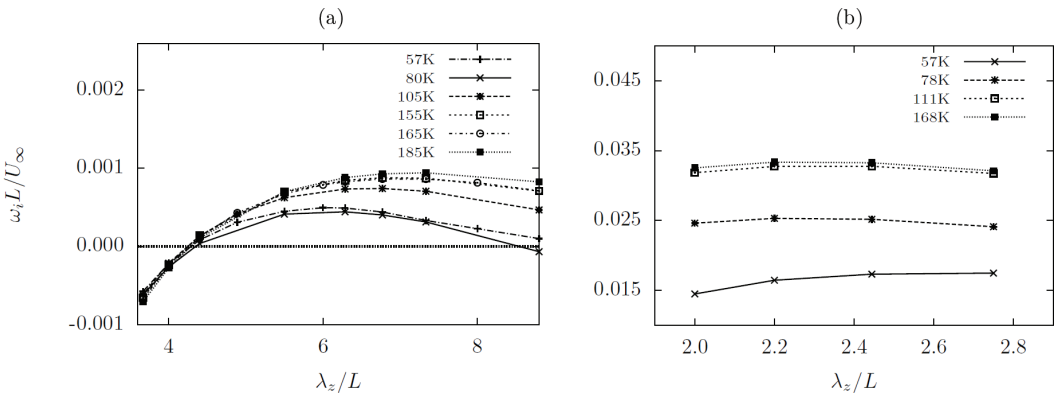

FIG. 26. Grid convergence of the growth rates for the (a) $\theta = 8^\circ$ and (b) $\theta = 10^\circ$ cases.

[1] J. Olejniczak, M. J. Wright, and G. V. Candler, Numerical study of inviscid shock interactions on double-wedge geometries, J. Fluid Mech. **352**, 1 (1997).
[2] A. Roghelia, H. Olivier, I. Egorov, and P. Chuvakhov, Experimental investigation of Görtler vortices in hypersonic ramp flows, Exp. Fluids **58**, 139 (2017).
[3] J. J. Ginoux, On some properties of reattaching laminar and transitional high speed flows, Von Karman Institute Report No. 53, 1969.
[4] G. Simeonides and W. Haase, Experimental and computational investigations of hypersonic flow about compression ramps, J. Fluid Mech. **283**, 17 (1995).
[5] V. I. Zapryagaev, I. N. Kavun, and I. I. Lipatov, Supersonic laminar separated flow structure at a ramp for a free-stream Mach number of 6, Prog. Flight Phys. **5**, 349 (2013).
[6] F. Schrijer, Investigation of Görtler vortices in a hypersonic double compression ramp flow by means of infrared thermography, Quant. Infrared Thermogr. J. **7**, 201 (2010).
[7] L. Yang, H. Zare-Behtash, E. Erdem, and K. Kontis, Investigation of the double ramp in hypersonic flow using luminescent measurement systems, Exp. Thermal Fluid Sci. **40**, 50 (2012).
[8] Y. Ishiguro, H. Nagai, K. Asai, and K. Nakakita, Visualization of hypersonic compression corner flows using temperature- and pressure-sensitive paints, *45th AIAA Aerospace Sciences Meeting and Exhibit, Reno, Nevada, 2007*, paper 2007-0118, doi:10.2514/6.2007-118.
[9] M. Bleilebens and H. Olivier, On the influence of elevated surface temperatures on hypersonic shock wave/boundary layer interaction at a heated ramp model, Shock Waves **15**, 301 (2006).
[10] R. Benay, B. Chanetz, B. Mangin, L. Vandomme, and J. Perraud, Shock wave/transitional boundary-layer interactions in hypersonic flow, AIAA J. **44**, 1243 (2006).
[11] S. Willems, A. Gülhan, and J. Steelant, Experiments on the effect of laminar-turbulent transition on the SWBLI in H2K at Mach 6, Exp. Fluids **56**, 49 (2015).
[12] G. R. Inger, Three-dimensional heat-and mass-transfer effects across high-speed reattaching flows, AIAA J. **15**, 383 (1977).
[13] L. De Luca, G. Cardone, D. A. De La Chevalerie, and A. Fonteneau, Viscous interaction phenomena in hypersonic wedge flow, AIAA J. **33**, 2293 (1995).
[14] D. A. de la Chevalerie, A. Fonteneau, L. De Luca, and G. Cardone, Görtler-type vortices in hypersonic flows: The ramp problem, Exp. Thermal Fluid Sci. **15**, 69 (1997).
[15] H. Görtler, On the three-dimensional instability of laminar boundary layers on concave walls, NACA Technical Memorandum No. 1375, 1954.
[16] P. Hall, The linear development of Görtler vortices in growing boundary layers, J. Fluid Mech. **130**, 41 (1983).
[17] S. Matsumura, S. P. Schneider, and S. A. Berry, Streamwise vortex instability and transition on the hyper-2000 scramjet forebody, J. Spacecr. Rockets **42**, 78 (2005).
[18] A. Roghelia, P. Chuvakhov, H. Olivier, and I. Egorov, Experimental investigation of Görtler vortices in hypersonic ramp flows behind sharp and blunt leading edges, *47th AIAA Fluid Dynamics Conference, Denver, 2017*, paper 2017–3463, doi:10.2514/6.2017-3463.
[19] Y. Zhuang, H.-J. Tan, Y.-Z. Liu, Y.-C. Zhang, and Y. Ling, High resolution visualization of Görtler-like vortices in supersonic compression ramp flow, J. Visual. **20**, 505 (2017).
[20] S. Priebe and M. P. Martín, Low-frequency unsteadiness in shock wave–turbulent boundary layer interaction, J. Fluid Mech. **699**, 1 (2012).
[21] S. Priebe, J. H. Tu, C. W. Rowley, and M. P. Martín, Low-frequency dynamics in a shock-induced separated flow, J. Fluid Mech. **807**, 441 (2016).
[22] L. M. Brown, R. R. Boyce, N. Mudford, and S. O'Byrne, in *Proceedings of the 16th AIAA/DLR/DGLR International Space Planes and Hypersonic Systems and Technologies Conference* (AIAA, Reston, 2009), Vol. 1, paper 7205-1.
[23] H. Görtler, Dreidimensionale instabilität der ebenen staupunktströmung gegenüber wirbelartigen störungen, in *50 Jahre Grenzschichtforschung*, edited by H. Görtler and W. Tollmien (Springer Vieweg, Braunschweig, 1955), p. 304.
[24] G. Hämmerlin, Zur instabilitätstheorie der ebenen staupunktströmung, in *50 Jahre Grenzschichtforschung* (Ref. [23]), p. 315.

[25] A. J. P. Fletcher, A. I. Ruban, and J. D. A. Walker, Instabilities in supersonic compression ramp flow, J. Fluid Mech. **517**, 309 (2004).
[26] K. W. Cassel, A. I. Ruban, and J. D. A. Walker, An instability in supersonic boundary-layer flow over a compression ramp, J. Fluid Mech. **300**, 265 (1995).
[27] A. Dwivedi, J. W. Nichols, M. R. Jovanovic, and G. V. Candler, Optimal spatial growth of streaks in oblique shock/boundary layer interaction, *Eighth AIAA Theoretical Fluid Mechanics Conference, Denver, Colorado*, paper 2017-4163, doi:10.2514/6.2017-4163.
[28] V. Theofilis, Global linear instability, Annu. Rev. Fluid Mech. **43**, 319 (2011).
[29] J.-C. Robinet, Bifurcations in shock-wave/laminar-boundary-layer interaction: Global instability approach, J. Fluid Mech. **579**, 85 (2007).
[30] N. Hildebrand, A. Dwivedi, J. W. Nichols, M. R. Jovanović, and G. V. Candler, Simulation and stability analysis of oblique shock-wave/boundary-layer interactions at Mach 5.92, Phys. Rev. Fluids **3**, 013906 (2018).
[31] V. Theofilis, S. Hein, and U. Dallmann, On the origins of unsteadiness and three-dimensionality in a laminar separation bubble, Philos. Trans. R. Soc. A **358**, 3229 (2000).
[32] D. Rodriguez and V. Theofilis, Structural changes of laminar separation bubbles induced by global linear instability, J. Fluid Mech. **655**, 280 (2010).
[33] F. Gallaire, M. Marquillie, and U. Ehrenstein, Three-dimensional transverse instabilities in detached boundary layers, J. Fluid Mech. **571**, 221 (2007).
[34] D. Barkley, M. Gabriela M. Gomes, and R. D. Henderson, Three-dimensional instability in flow over a backward-facing step, J. Fluid Mech. **473**, 167 (2002).
[35] G. A. Bres and T. Colonius, Three-dimensional instabilities in compressible flow over open cavities, J. Fluid Mech. **599**, 309 (2008).
[36] R. Caljouw, An experimental investigation of a three-dimensional hypersonic flow on a double ramp geometry using stereo-PIV, Master's thesis, Delft University of Technology, 2007 .
[37] A. M. Knisely and J. M. Austin, Geometry and test-time effects on hypervelocity shock-boundary layer interaction, *54th AIAA Aerospace Sciences Meeting, San Diego, California*, paper 2016-1979, doi:10.2514/6.2016-1979.
[38] J. R. Komives, I. Nompelis, and G. V. Candler, Numerical investigation of unsteady heat transfer on a double wedge geometry in hypervelocity flows, *44th AIAA Fluid Dynamics Conference*, paper 2014-2354, doi:10.2514/6.2014-2354.
[39] I. Nompelis and G. V. Candler, Numerical investigation of double-cone flows with high enthalpy effects, in *Proceedings of the Sixth European Symposium Aerothermodynamics for Space Vehicles*, edited by L. Ouwehand (European Space Agency, Noordwijk, 2009).
[40] S. GS, A. Dwivedi, G. V. Candler, and J. W. Nichols, Global linear stability analysis of high speed flows on compression ramps, *47th AIAA Fluid Dynamics Conference, Denver, 2017*, paper 2017–3455.
[41] A. Sansica, N. D. Sandham, and Z. Hu, Forced response of a laminar shock-induced separation bubble, Phys. Fluids **26**, 093601 (2014).
[42] A. Sansica, N. D. Sandham, and Z. Hu, Instability and low-frequency unsteadiness in a shock-induced laminar separation bubble, J. Fluid Mech. **798**, 5 (2016).
[43] A. Dwivedi, S. GS, G. V. Candler, J. W. Nichols, and M. R. Jovanović, Input-output analysis of shock boundary layer interaction, *48th AIAA Fluid Dynamics Conference, Atlanta, Georgia*, 2018, paper 2018-3220, doi:10.2514/6.2018-3220.
[44] D. R. Lindquist and M. B. Giles, Validity of linearized unsteady Euler equations with shock capturing, AIAA J. **32**, 46 (1994).
[45] E. Kreiselmaier and B. Laschka, Small disturbance Euler equations: Efficient and accurate tool for unsteady load prediction, J. Aircr. **37**, 770 (2000).
[46] C. J. Mack and P. J. Schmid, A preconditioned Krylov technique for global hydrodynamic stability analysis of large-scale compressible flows, J. Comput. Phys. **229**, 541 (2010).
[47] K. C. Hall, W. S. Clark, and C. B. Lorence, in *Proceedings of the ASME 1993 International Gas Turbine and Aeroengine Congress and Exposition* (American Society of Mechanical Engineers, New York, 1993), paper V001T03A035.

[48] R. W. MacCormack, *Numerical Computation of Compressible and Viscous Flow* (AIAA, Reston, 2014).
[49] R. W. MacCormack and G. V. Candler, The solution of the Navier-Stokes equations using Gauss-Seidel line relaxation, Comput. Fluids **17**, 135 (1989).
[50] P. K. Subbareddy and G. V. Candler, A fully discrete, kinetic energy consistent finite-volume scheme for compressible flows, J. Comput. Phys. **228**, 1347 (2009).
[51] P. K. Subbareddy, M. D. Bartkowicz, and G. V. Candler, Direct numerical simulation of high-speed transition due to an isolated roughness element, J. Fluid Mech. **748**, 848 (2014).
[52] C. Zhang and R. J. LeVeque, The immersed interface method for acoustic wave equations with discontinuous coefficients, Wave Motion **25**, 237 (1997).
[53] J. Piraux and B. Lombard, A new interface method for hyperbolic problems with discontinuous coefficients: One-dimensional acoustic example, J. Comput. Phys. **168**, 227 (2001).
[54] T. R. Fogarty and R. J. LeVeque, High-resolution finite-volume methods for acoustic waves in periodic and random media, J. Acoust. Soc. Am. **106**, 17 (1999).
[55] S.-E. Kim, B. Makarov, and D. Caraeni, A multi-dimensional linear reconstruction scheme for arbitrary unstructured grids, *16th Computational Fluid Dynamics Conference, Orlando, 2003*, paper 2003–3990.
[56] E. Shima, K. Kitamura, and T. Haga, Green-gauss/weighted-least-squares hybrid gradient reconstruction for arbitrary polyhedra unstructured grids, AIAA J. **51**, 2740 (2013).
[57] I. Nompelis, T. W. Drayna, and G. V. Candler, *Parallel Computational Fluid Dynamics 2005* (Elsevier, Amsterdam, 2006), pp. 389–395.
[58] R. B. Lehoucq, D. C. Sorensen, and C. Yang, *ARPACK Users' Guide: Solution of Large-Scale Eigenvalue Problems with Implicitly Restarted Arnoldi Methods* (SIAM, Philadelphia, 1998).
[59] X. S. Li and J. W. Demmel, SuperLU_DIST: A scalable distributed-memory sparse direct solver for unsymmetric linear systems, ACM Trans. Math. Software **29**, 110 (2003).
[60] I. Nompelis, G. V. Candler, and M. S. Holden, Effect of vibrational nonequilibrium on hypersonic double-cone experiments, AIAA J. **41**, 2162 (2003).
[61] P. Bookey, C. Wyckham, and A. J. Smits, Experimental investigations of Mach 3 shock-wave turbulent boundary layer interactions, *35th AIAA Fluid Dynamics Conference and Exhibit*, paper 2005–4899.
[62] J.-P. Dussauge, P. Dupont, and J.-F. Debiève, Unsteadiness in shock wave boundary layer interactions with separation, Aerosp. Sci. Technol. **10**, 85 (2006).
[63] B.-T. Chu, On the energy transfer to small disturbances in fluid flow (part I), Acta Mech. **1**, 215 (1965).
[64] K. J. George and R. I. Sujith, On Chu's disturbance energy, J. Sound Vib. **330**, 5280 (2011).
[65] P. J. Schmid and L. Brandt, Analysis of fluid systems: Stability, receptivity, sensitivity: Lecture notes from the FLOW-NORDITA summer school on advanced instability methods for complex flows, Stockholm, Sweden, 2013, Appl. Mech. Rev. **66**, 021003 (2014).
[66] F. Giannetti and P. Luchini, Structural sensitivity of the first instability of the cylinder wake, J. Fluid Mech. **581**, 167 (2007).
[67] D. Sipp and L. Jacquin, Three-dimensional centrifugal-type instabilities of two-dimensional flows in rotating systems, Phys. Fluids **12**, 1740 (2000).
[68] M. R. Malik, Numerical methods for hypersonic boundary layer stability, J. Comput. Phys. **86**, 376 (1990).
[69] V. Theofilis and T. Colonius, An algorithm for the recovery of 2- and 3D biglobal instabilities of compressible flow over 2D open cavities, *33rd AIAA Fluid Dynamics Conference and Exhibit, Orlando, Florida*, paper 2003-4143, doi:10.2514/6.2003-4143.
[70] S. Mittal, Stability of flow past a cylinder: Energy budget of eigenmodes, Int. J. Numer. Methods Fluids **63**, 533 (2010).
[71] D. Fabre, L. Jacquin, and J. Sesterhenn, Linear interaction of a cylindrical entropy spot with a shock, Phys. Fluids **13**, 2403 (2001).